The Extended Timing Annotation Dataset for Sentinel-1 – Product Description and First Evaluation Results

Christoph Gisinger, Ludivine Libert, Petar Marinkovic, Lukas Krieger, Yngvar Larsen, Antonio Valentino, Helko Breit, Ulrich Balss, Steffen Suchandt, Thomas Nagler, *Member, IEEE*, Michael Eineder, *Fellow, IEEE*, Nuno Miranda

***Abstract*—This paper introduces the extended timing annotation dataset (ETAD) product for Sentinel-1 (S-1) which was developed in a joint effort of German Aerospace Center (DLR) and the European Space Agency (ESA). It allows to correct range and azimuth timing of S-1 images for geophysical effects as well as for inaccuracies in synthetic aperture radar (SAR) image focusing. In combination with the precise orbit solution, these effects determine the absolute geolocation accuracy of S-1 SAR images and the relative collocation accuracy of repeat pass image stacks. ETAD contains the gridded timing corrections for the tropospheric and ionospheric path delays, the tidal-based surface displacements, and the SAR processing effects, all of which are computed for each data take using standard models from geodesy and auxiliary atmospheric data. The ETAD product helps S-1 users to significantly improve the geolocation accuracy of the S-1 SAR products to better than 0.2 m and offers a potential solution for correcting large scale interferometric phase variations. The product layout and the product generation are described schematically. The paper also reports first results for different SAR techniques: first, the improvement in geolocation accuracy down to a few centimeters by verification of accurately surveyed corner reflector positions in the range-azimuth plane; second, the well-established offset-tracking technique, that is used for systematic ice velocity monitoring of ice sheets and glaciers, where ETAD can reduce velocity biases down to sub-centimetric values; and third, the correction of atmospheric phase contributions in wide-area interferograms used for national and European ground motion services. These early results proof the added value of the ETAD corrections and that the product design is well suited to be integrated into the processing flows of established SAR applications such as absolute ranging of targets, speckle/feature tracking and interferometry.**

***Index Terms*—Radar remote sensing, Sentinel-1, imaging geodesy, SAR geodesy, synthetic aperture radar, speckle tracking, InSAR, atmospheric phase screen, ionospheric phase screen, glaciology, natural hazards**

The work was funded by the EU Commission's Copernicus Programme through the ESA contract 4000126567/19/I-BG.

C. Gisinger, L. Krieger, H. Breit U. Balss, and S. Suchandt are with the Remote Sensing Technology Institute, German Aerospace Center, 82234 Wessling, Germany (e-mail: christoph.gisinger@dlr.de).

L. Libert and T. Nagler are with the Environmental Earth Observation Information Technology (ENVEO IT) GmbH, 6020 Innsbruck, Austria.

P. Marinkovic is with PPO.labs, The Hague, The Netherlands.

Y. Larsen is with NORCE, 9294 Tromsø, Norway.

M. Eineder is with the Remote Sensing Technology Institute, German Aerospace Center, 82234 Wessling, Germany, and with the Technical University of Munich, 80333 Munich, Germany.

A. Valentino and N. Miranda are with the European Space Agency, 00044 Frascati, Italy.

NOMENCLATURE

ALE	absolute location error
API	Application Programming Interface
APS	atmospheric phase screen
C3S	Copernicus Climate Change Service
CR	corner reflector
DEM	digital elevation model
DLR	German Aerospace Center
ECMWF	European Centre for Medium-Range Weather Forecasts
ESA	European Space Agency
ETAD	extended timing annotation dataset
EW	Extended Wide swath
FM	frequency modulation
GNSS	global navigation satellite system
IGS	International GNSS Service
IPP	ionospheric pierce point
ITRF	International Terrestrial Reference Frame
IV	ice velocity
IW	Interferometric Wide swath
NWM	numerical weather model
OT	offset-tracking
RMS	root mean square
S-1	Sentinel-1
S-1A	Sentinel-1A
S-1B	Sentinel-1B
SETAP	Sentinel-1 Extended Timing Annotation Processor
SAR	synthetic aperture radar
SCR	signal to clutter ratio
SLC	single look complex
SM	Stripmap
TEC	total electron content
TOPS	Terrain Observation with Progressive Scan
UTC	Coordinated Universal Time

I. INTRODUCTION

SAR sensors have an intrinsically high pixel localization accuracy because the position in a SAR image is governed by the timing of actively transmitted pulses and recorded radar echoes [1], [2]. The SAR range distance is inferred from the echo runtime which can be determined readily with a precision corresponding to centimeters or even millimeters, depending

on the quality of the oscillator [3], [4]. The azimuth localization is determined by the synthetic aperture, i.e., the flight track and the referencing of the SAR clock to the orbit time. It could be determined down to millimeters but is currently often limited to decimeters due to the lack of precision in absolute time referencing. When converting these highly precise range and azimuth time measurements to space coordinates, the wave propagation through the neutral troposphere and the dispersive ionosphere, and the uncertainty on the orbit position are the dominating error sources.

As known from comparisons with tropospheric path delays observed with global navigation satellite system (GNSS) technology, the propagation delay can be computed with an accuracy of a few centimeters by integration of numerical weather models [5]–[8], and the ionospheric state can be defined by physical models or inferred from observations of global GNSS networks [9]–[11], allowing for the correction of ionospheric path delays in single-frequency microwave data. As for the orbit position, even 25 years ago satellite orbit state vectors could be determined with 7 cm radial root mean square (RMS) and 30 cm along-track RMS [12], and can be determined with 2-3 cm position accuracy today [13]–[16]. However, the geometric accuracy of SAR systems was not fully exploited so far. This might be due to the lack of requirements on the geometric SAR products and the consequent lack of thorough analysis and algorithm design, that were in contrast developed by the GNSS community, see for instance Teunissen and Montenbruck, 2017 [17]. For the sake of conciseness, we list here only the main contributions and error sources that are neglected in most of the currently available operational SAR products: atmospheric propagation delay through troposphere and ionosphere (2-4 m); inaccurate azimuth time referencing between SAR and GNSS clock (0.2 m); SAR focusing inaccuracies such as stop-go-approximation (< 3 m); implications of GNSS-based orbit determination and the geo-dynamic deformations associated with the underlying geodetic reference frames (< 0.2 m). A more detailed explanation can be found in [18]–[21], where it is shown that a breakthrough in geometric accuracy can only be achieved if all the aforementioned affects are considered properly.

In consequence, ESA and DLR investigated the technical capabilities of S-1 mission and the design of a S-1-based SAR product with geodetic accuracy. The results are the calibration procedures described in [22] and the very promising results published in [23]. Based on this initial analysis, the ETAD product was designed. The goal of ETAD is to provide a wide range of users with a product easy to use, so they can benefit from the geodetic accuracy of SAR without dealing with the details of the SAR processing technology and the standards and techniques used in geodesy. The product is designed as a correction layer to be applied by the user, which avoids the modification of the original SAR data distributed by ESA and leaves the possibility to consistently apply the corrections to datasets derived from the original SAR scenes as delivered by ESA. The algorithms have been implemented into an operational software for the S-1 ground segment that can be potentially used to generate correction data for every scene acquired by the S-1A/B fleet.

In subsequent pilot studies, the ETAD product has been tested and validated for two S-1-based products of operational services: the monitoring of the Greenland ice sheet flow velocity applying SAR offset-tracking (OT), and ground motion monitoring in Norway with SAR interferometry. OT is a technique that aims at estimating the local shifts between two SAR images, that are mostly related to ice motion when observing glaciers and ice caps [24]–[27]. However, these offsets are impacted by uncorrected timing delays, especially for ice caps at high latitudes where the ionosphere can introduce severe shifts in the SAR data. ETAD constitutes a promising solution for correcting timing-related biases in S-1 OT measurements, and its use is investigated in the case of the ice velocity monitoring over the Greenland ice sheet.

The second application is ground motion mapping using SAR interferometry. Spatially correlated atmospheric phase screens are the most dominant error source in interferometry. Extensive workshops and studies have been performed by UNAVCO/US [28] and ESA [29], trying to reduce the atmospheric phase screen with numerical weather models (NWMs) and data driven methods. The general conclusion was that NWMs do currently not provide the resolution and accuracy to reliably correct high-resolution SAR interferograms. The 10 km horizontal resolution of the operational Integrated Forecast System (IFS) analysis data from the European Centre for Medium-Range Weather Forecasts (ECMWF) [30], which we use as background data, is indeed insufficient for high-resolution phase correction. Instead, our ETAD product targets on tropospheric phase errors with correlation lengths larger than 50 km and on systematic errors caused by changing atmospheric refraction in areas with significant topography. We tested this ability on large area interferograms in Norway which are used for the national ground motion service and the upcoming European Ground Motion Service (EGMS). Even if the ETAD product was primarily defined for centimetric range/azimuth corrections, the range component can be used to model tropospheric delay variations and reduce stratified phase errors in interferograms with convincing results.

The paper is structured as follows: Chapter II introduces the architecture of the ETAD product and the algorithms to generate it. The validation of ETAD applying SAR geolocation was carried out by DLR and is reported in chapter III. In the chapters IV and V, we report on the first demonstration and the independent assessment of ETAD in ice velocity monitoring and SAR interferometry performed by ENVEO and PPO.labs, respectively, who were not involved in the product development. Finally, chapter VI summarizes key aspects and provides an outlook on the operational generation of ETAD products by ESA.

II. The ETAD Product

A. Features and Contents

The S-1 single look complex (SLC) image products are processed for the zero-Doppler geometry convention [31]. Consequently, the 2-D coordinates annotated to the SAR images, slant range time τ and azimuth time t, describe an

TABLE I
ACCURACY SPECIFICATION OF ETAD CORRECTIONS AND NOMINAL LOCATION ACCURACY SPECIFICATION OF S-1 SLC PRODUCTS [31], [33].

SAR mode	ETAD products (1 sigma)		S-1 SLC products (3 sigma)	
	Rg [m]	Az [m]	Rg [m]	Az [m]
TOPS IW	0.2	0.1	7.0	7.0
Stripmap	0.2	0.1	2.5	2.5

orthogonal raster for which every range line of positions on the ground $\mathbf{X}$ corresponds to a single azimuth time t linked to the sensor's state vector $\mathbf{X}_s(t), \dot{\mathbf{X}}_s(t)$. This is summarized by the SAR range Doppler equations in zero-Doppler configuration [2], [32]:

$$\tau = 2/c \cdot |\mathbf{X}_s(t) - \mathbf{X}| \tag{1}$$

$$0 = \frac{\dot{\mathbf{X}}_s(t)\,(\mathbf{X}_s(t) - \mathbf{X})}{|\dot{\mathbf{X}}_s(t)|\,|\mathbf{X}_s(t) - \mathbf{X}|} \tag{2}$$

where c denotes the speed of light in vacuum. The fulfillment of these equations by a SLC image product with respect to the true positions on the ground defines the geolocation quality and thus the geometric fidelity of the SAR system. For the S-1 products demanding near real time processing and distribution, the nominal specification of absolute geolocation accuracy is listed in Table I, which does not involve any additional timing corrections for path delays or surface deformation. Improving the meter level geolocation accuracy to well below sub-meter level and maximizing the geometric fidelity of operational S-1 products is the main goal of the ETAD product and its timing corrections. The overall accuracy of ETAD corrections (1 sigma) at a global level is specified with 0.2 m range and 0.1 m azimuth, see Table I. These numbers are based on the accuracy of the used correction methods and the underlying input data, see chapter II-B. It is important to note that the absolute geolocation accuracy evaluates the entire SAR system, involving effects not controlled by the ETAD product, e.g., SAR antenna phase center offset, finite azimuth time quantization or oscillator aging. Therefore, the formal ETAD specifications apply only to the standalone product and do not specify an attainable geolocation accuracy of S-1 SLC products. However, the validation results documented in this publication show that in practice the S-1 SAR system can even exceed these specifications when applying ETAD corrections.

The ETAD product is directly computed from the annotations of S-1 level 1 SLC products and auxiliary data comprising the precise orbit files, atmospheric model data and the solid earth tide model, which are described in section II-B. This allows the generation of extended timing corrections for every S-1 SLC acquisition in the catalog. At the time of writing, the product has a latency of 21 days after an acquisition because of the usage of the S-1 precise orbit solution. Currently, the ETAD product is qualified for the two S-1 modes Interferometric Wide swath (IW) and Stripmap (SM) [31], but the processing of Extended Wide swath (EW) mode is already possible at an experimental level. The detailed ETAD format specification is available from ESA [34].

The ETAD product contains slant-range and azimuth timing corrections for tropospheric delays, ionospheric delays, solid earth tides, the S-1 system effects stemming from the SAR processing, as well as instrument calibration constants. It is delivered in the Standard Archive Format for Europe (SAFE) structure [35]. The product contains the extracted precise orbit segment specific to the data take, a quicklook file and the two core ETAD components: the ETAD NetCDF product and the ETAD XML product. The ETAD XML product provides fast access to the grid definitions of the individual bursts and contains statistics for the timing corrections of each burst. In addition, it contains auxiliary information about processing parameters and lists the used input data products.

The NetCDF product provides the correction data grids. It is a self-contained file that has all necessary information for the application of corrections of SLC SAR timings or the generation of InSAR phase screens. It defines a grid equally spaced in time which encompasses the entire S-1 data take and which is annotated by fast time τ (range) and slow time t (azimuth). Depending on the SAR mode of the corresponding S-1 SLC product, the NetCDF contains a number of groups equal to the number of swathes acquired in this mode. These swath groups contain subgroups for each burst. Consequently, the internal structure is closely following the underlying SAR SLC data [31], see Fig. 1. For SM acquisitions, an entire SM slice is treated as a single burst. The reason for this burst-wise handling of corrections are the S-1 system corrections which differ in overlapping bursts and swaths.

The NetCDF burst groups contain the individual corrections in 7 NetCDF layers as shown in Fig. 3, plus two additional layers for the sum of range and sum of azimuth corrections. The range and azimuth times of the correction grid nodes are annotated in two vectors. Moreover, 3 layers define the corresponding latitude, longitude and height coordinates of the grid points. It has to be noted that the sum layers already contain the timing calibration constants for the sensor. All the timing corrections are given in units of seconds. Additional information, e.g. for selecting a subset of corrections or to transform the timing corrections into metric shifts are annotated as attributes of the respective NetCDF groups [34].

The achievable accuracy when applying the ETAD timing corrections is driven by the entire S-1 system, which also involves any bias stemming from internal electronic delays, polarization-dependent biases, orbit errors, or potential biases of the applied geophysical corrections. Consequently, the ETAD product generation uses a sensor calibration for range and azimuth timings, which accounts for the overall system biases and which has to be determined empirically. The initial values of the used auxiliary file stem from a calibration that DLR performed at the Metsähovi calibration site, Finland, with 3 years of S-1A and S-1B IW data (2017-2020) and corrections according to the ETAD methods. The Metsähovi station contains a very stable corner reflector (CR) with 1.5 m edge length, which was also used for the accurate geometric recalibration of the TerraSAR-X mission [21]. For the details on accurate geometric SAR calibration see [22], [23]. The

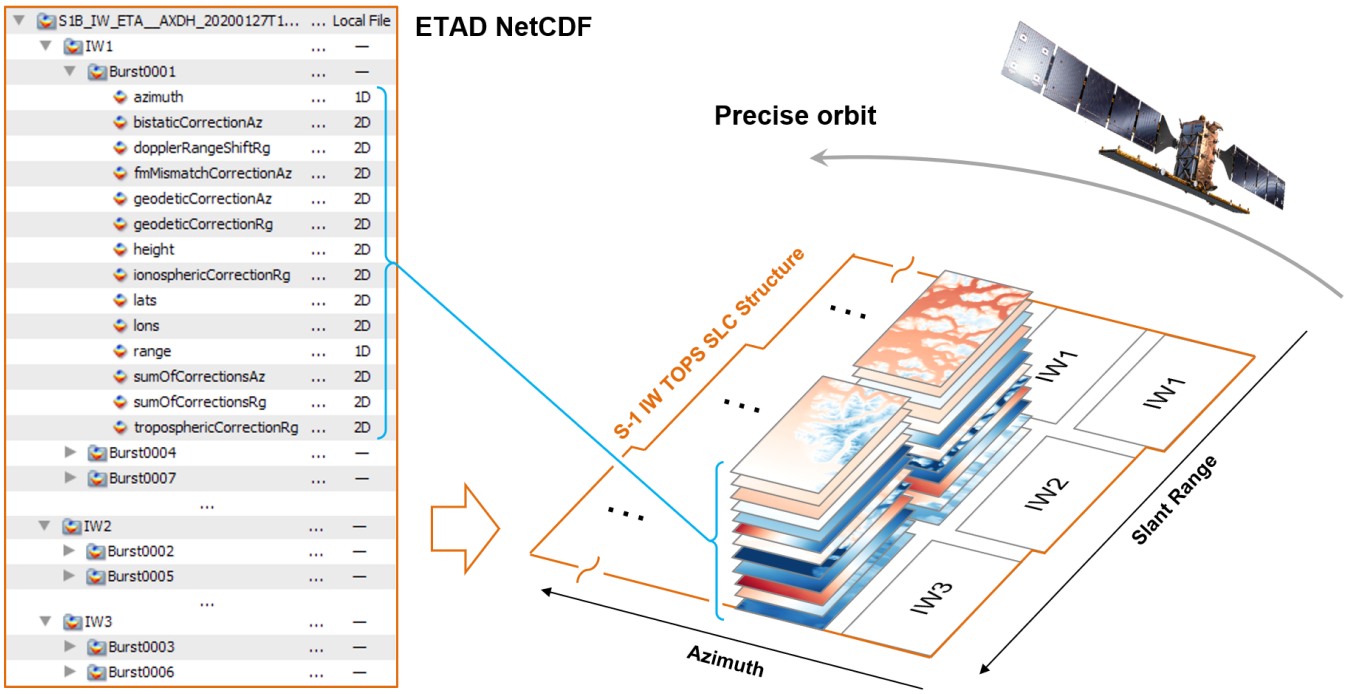

Fig. 1. The ETAD NetCDF product is structured hierarchically in groups for each sub-swath and burst which contain a stack of 9 correction grids and 3 coordinate grids. The individual burst correction grids lie on a continuous range and azimuth time grid encompassing the whole data take. The range and azimuth times defining the grid of a given burst are annotated as 1D vectors.

TABLE II
INITIAL SENTINEL-1 TIMING CALIBRATION CONSTANTS FOR S-1 ETAD PRODUCT AND CORRESPONDING NUMBERS IN UNITS OF METERS.

Sensor	$\Delta\tau_{cal}$ [s]	Δt_{cal} [s]	Rg [m]	Az [m]
S1A	$1.1281e^{-9}$	$1.2873e^{-5}$	0.1691	0.0875
S1B	$0.0646e^{-9}$	$-4.9701e^{-5}$	0.0097	−0.3380

initial calibration contains numbers for range and azimuth and S-1A and S-1B, respectively, which are used for all SAR modes, beams and polarizations, see Table II. Maintenance will be carried out by the S-1 Mission Performance Cluster that regularly performs sensor and product evaluations [36]. The applied timing calibration values are also annotated in the ETAD product NetCDF and are completely transparent to the user.

B. Algorithms and Processing Chain

The Sentinel-1 Extended Timing Annotation Processor (SETAP) software was implemented according to S-1 ground segment requirements to generate ETAD products on an operational basis. The computations are based on the sliced S-1 level 1 SLC products forming a data take [31]. They are provided to the processor along with the S-1 precise orbit ephemeris product, see the schematic workflow shown in Fig. 2. For performance optimization, steps that refer to data take slices and bursts are run concurrently. A crucial step is to define a correction grid that consistently covers all provided input data. The grid is calculated in range and azimuth as two-way times and as delta times in seconds with respect to a minimum ETAD product Coordinated Universal Time (UTC) time, respectively. The spacing is predefined and corresponds on average to a 200 m ground sampling in both dimensions. The grid of radar timings is geolocated on a digital elevation model (DEM), i.e., the Copernicus 90m DEM, [37], to define the 3-D sensor-to-ground geometry, and the geoid model EGM2008 (Earth Gravitational Model 2008, [38]) is imported as well at this point for converting the mean sea level referenced DEM heights to ellipsoidal heights (WGS-84, [39]). With the satellite positions and the 3-D coordinates of the computational grid known, the ETAD corrections are computed with the methods described below, for which additional details can be found in our earlier publications [7], [21], [23] and in the processor algorithm technical baseline document [40]. Note that the corrections for tropospheric and ionospheric delays, solid Earth tides, and the bistatic azimuth correction are computed for all S-1 input products, whereas the corrections for Doppler shifts in range and FM-rate mismatch shifts in azimuth only apply to the TOPS mode data [23]. Results of the different corrections are shown in Fig. 3 for a S-1 data take acquired over Alaska, USA.

1) Direct Integration of NWM for Tropospheric Delays: The tropospheric delay is retrieved by numerical integration of air refractivity modelled along the geometrical line-of-sight between the sensor and the grid point on ground. For the steep to medium incidence angles of S-1 acquisitions (20 ° - 45 °), there is no need to consider the additional ray bending effect because its contribution reaches only a few millimeters at the most [41]. The total tropospheric delay is on the order

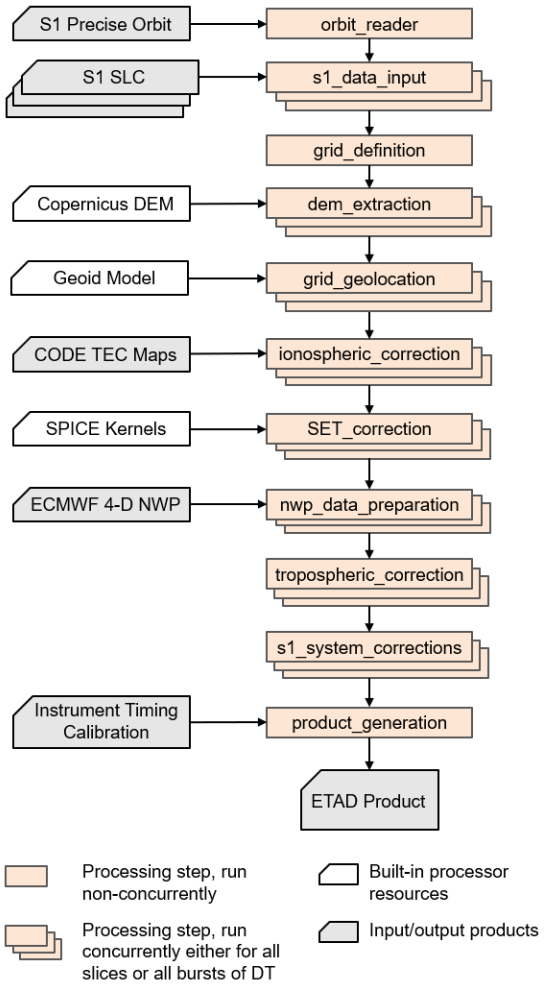

Fig. 2. SETAP processing chain with the steps for correction calculation as well as for preparation of the input data. For performance optimization, several parts of the processor are run con-currently either on the S1 input data take slices or bursts.

of 2 to 4 m, depending on terrain height and local incidence angle. The air refractivity can be expressed as a function of temperature T, pressure P and specific humidity q. All three parameters are available in the analysis data of the operational integrated forecast system (IFS) model of ECMWF in 6-hour time intervals (00h, 06h, 12h, 18h UTC) in 3-D, i.e., as a number of 137 vertically stacked 2-D layers (model levels) with a horizontal spatial resolution of approximately 10 km [30], [42]. The direct integration is carried out over discrete intervals ΔR in line-of-sight direction and between z_g and $z_{ML,top}$, the mean sea level heights of the grid point and of the top model layer, respectively, requiring the involved NWM data to be properly interpolated horizontally and vertically for each integration step n:

$$SPD_{tro} = 10^{-6} \sum_{n} \left(k_1 \frac{P_n}{T_n} + k_2^{'} \frac{e_n}{T_n} + k_3 \frac{e_n}{T_n^2} \right) \Delta R \quad \text{for} \quad n \mid z_g \leq z_n \leq z_{ML,top} \tag{3}$$

with $e_n \cong q_n P_n/\varepsilon$, $\varepsilon = R_d/R_w$, $R_d = 287.0\,\mathrm{JK^{-1}kg^{-1}}$, $R_w = 461.51\,\mathrm{JK^{-1}kg^{-1}}$ (gas constants for 1 kg of dry air and of water vapor, respectively [43]), $k_2^{'} = (k_2 - \varepsilon k_1)$, $k_1 = 0.776\,\mathrm{KPa^{-1}}$, $k_2 = 0.715\,\mathrm{KPa^{-1}}$ and $k_3 = 3750\,\mathrm{K^2Pa^{-1}}$ [7], [44]. The integration is performed for the NWM time instants that most closely precede and succeed the grid point's azimuth time. The two slant-path delay results are then linearly interpolated for the given grid time t_g and the outcome is converted to a two-way slant range delay using the speed of light in vacuum:

$$\Delta\tau_{tro} = SPD_{tro,t_g} \cdot 2/c. \tag{4}$$

In an earlier study, we validated the ECMWF-based path delays computed with the described method against GNSS-based path delays observed with the global GNSS network [7], which agree within 1-2 cm for most mid- to high-latitude stations and within 2-4 cm for stations in the equatorial region. These findings are in line with other published results on tropospheric path delays derived from ECMWF data [5], [6], [8].

2) Ionospheric Delay Computation from GNSS-based TEC Maps: Free electrons and charged particles in the ionosphere cause frequency-dependent path delays for microwave signals. Global ionospheric maps derived from GNSS observations of the global International GNSS Service (IGS) network define the state of the ionosphere by the vertical total electron content (TEC) condensed to a single spherical layer [9], [45]. The SETAP uses as input the daily sets of TEC maps $E_{vTEC}(\Phi, \lambda)$, horizontally referenced to geocentric latitude Φ and longitude λ with a resolution of 2.5 by 5 degrees, which are provided by the CODE (Center of Orbit Determination in Europe) in the framework of IGS [46]. The TEC can be readily scaled to frequency-dependent delays of the S-1 C-band by applying the equation (5). For a given correction grid point, the vTEC is interpolated at the location of the ionospheric pierce point (IPP), defined as the line-of-sight intersection with the spherical model layer. The temporal vTEC interpolation for the grid point's azimuth times t_g considers the time difference of the grid with respect to the two used TEC maps (before and after data acquisition). The result is the ionospheric delay in slant-range in units of seconds, which is obtained as

$$\Delta\tau_{ion} = \frac{2 \cdot C_I}{c \cdot f_{S1}^2 \cdot \cos(z')} \cdot E_{vTEC}(\Phi_{IPP}, \lambda_{IPP}, t_g) \cdot \alpha, \tag{5}$$

here C_I being the TEC proportionality factor $40.3 \cdot 10^{16}\,\mathrm{m^3 s^{-2}}$ [47], E_{vTEC} is the vertical TEC model interpolated in space and time, c the speed of light in vacuum, f_{s1} the S-1 radar frequency in Hertz, and $\cos(z')$ is the ionospheric mapping function depending on IPP zenith angle. The ionospheric delay may reach up to 1 m for the S-1 C-Band.

Moreover, the algorithm has to account for the fact that the S-1 orbit, having an altitude of around 712 km, is still within the upper region of the ionosphere. The equation therefore contains an additional parameter $\alpha = 0.9$ to reduce the GNSS-based vTEC that comprises the entire ionosphere. The empirical value is based on an earlier analysis performed with TerraSAR-X [21], and was adjusted for S-1. This constant scaling parameter can only approximate the fraction of the electron concentration applicable for S-1 data, but the impact

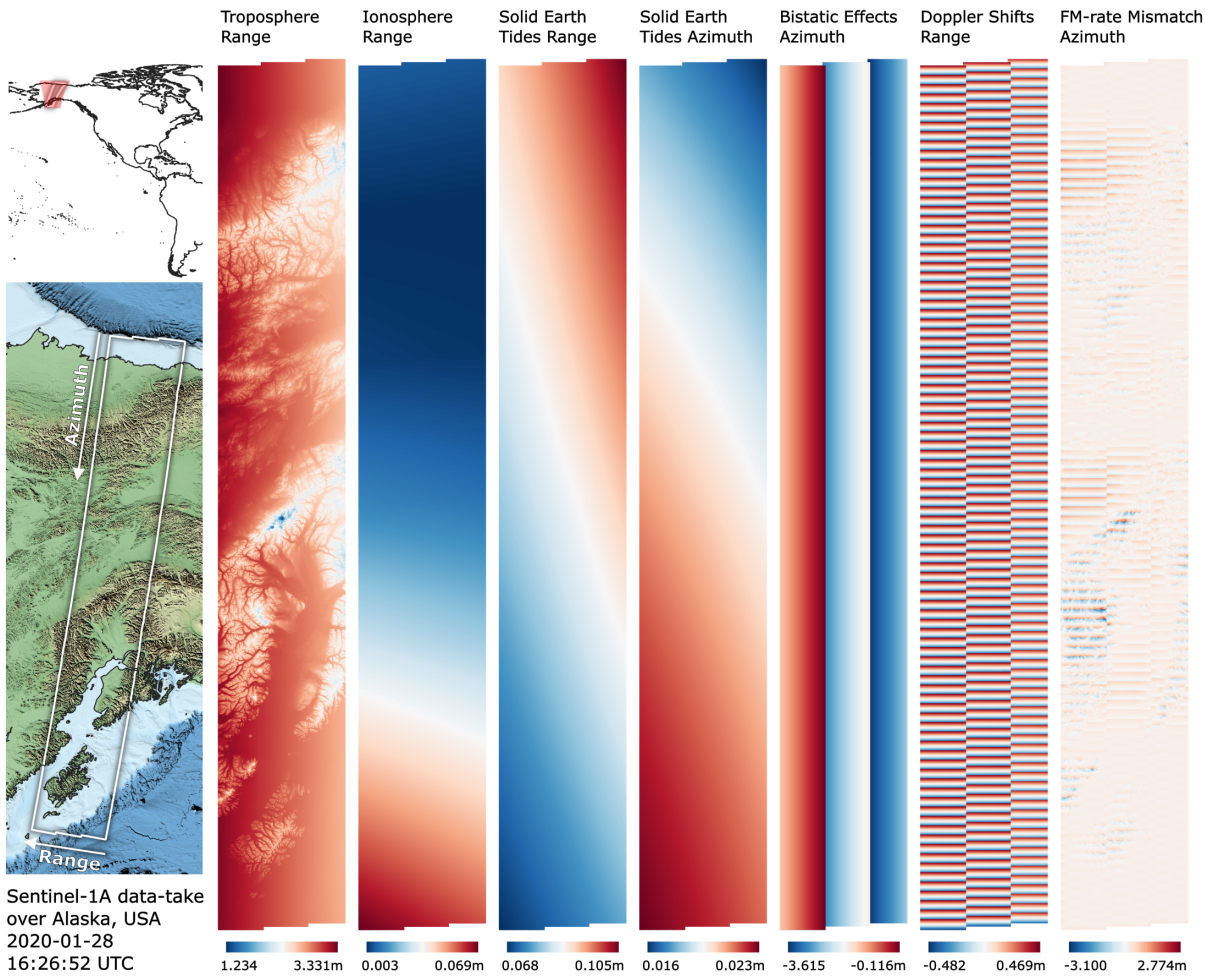

Fig. 3. Visualisation of the seven ETAD correction layers contained in the NetCDF product for a S-1A data take acquired over Alaska, USA. Timing corrections converted to units of meters by speed of light in vacuum divided by two (range corrections) and the zero-Doppler beam velocity (azimuth corrections).

is considered small and the applied scaling remains transparent to users as the parameter is also given in the ETAD product annotation.

The accuracy of the computed ionospheric delays reflects the station distribution and resolution of the IGS GNSS network providing the TEC data. The estimated spatial quality is published along with each solution and qualitative assessments show an accuracy of 4-5 TECU over open ocean and 1-2 TECU over most land areas [9]. This corresponds to 7-8 cm and 2-3 cm, respectively, in slant range C-band SAR data.

3) Solid Earth Tidal Displacement Computation: Solid Earth tides are deformations of the Earth crust caused by the gravitational force of the Sun and the Moon. The signal typically varies between $\pm 25\,\mathrm{cm}$ in vertical direction, but there is also a significant horizontal displacement of up to 6 cm [48]. At a global scale, which is the focus of the ETAD product, the direct tides are the dominating solid Earth displacement signal, but one should be aware that there are also ocean tide loading effects that can reach several centimeters at certain coastal regions [48].

The tides computation requires the time-dependent constellation of the Sun and the Moon as seen from the Earth, as well as a geodynamic model describing the deformation ability of the solid Earth. The model applied in ETAD is the conventional model of the International Terrestrial Reference Frame (ITRF) which is described in detail by the conventions associated with geodetic reference frames [48]. For the position vectors of Sun and Moon, the conventions refer to the D421 planetary ephemerides issued by NASA's Jet Propulsion Laboratory (JPL). These are retrieved using NASA's SPICE toolkit Application Programming Interface (API) [49]. The 3-D tidal displacement vector is obtained in units of meters in the global ITRF. Thus, the result requires a conversion into slant-range and azimuth timing geometry of the correction grid. This is done by computing the zero-Doppler radar times of the grid position including the tidal displacement and calculating the difference to the grid nominal radar times. Single Sentinel-1 SAR acquisitions can span several thousands of kilometers in North-South direction, see Fig. 3, for which the tidal effect within one data take may vary up to 20 cm in slant-range (peak-to-peak). For repeated acquisitions, the SAR data time series will eventually observe shifts of the Earth surface that have up to 25 cm amplitude.

The tide model considers all signal components with con-

tributions larger than 1 mm and can be considered inherently accurate because it is firmly embedded in the crust-based ITRF [48]. The frame conventions are also applied for the generation of the S-1 precise orbit solution [13]. Therefore, we remove the high-frequency time variations of the solid Earth tides but we do not apply any additional correction for secular surface deformations such as tectonics. This means that users will be able to observe signals of tectonic deformations and comparison with reference targets require proper consideration of the ITRF epoch [23].

4) Bistatic Azimuth Effects Mitigation: The motion of the S-1 satellites between pulse transmission and echo reception amounts to approximately 30-40 m. This quasi-bistatic situation is commonly neglected as SAR focusing schemes apply the stop-and-go approximation: it is assumed that the satellite stops between transmission and reception of a single pulse and only moves after each cycle [1]. This is beneficial with respect to computational efficiency, but the implications have to be carefully considered in order to generate SAR images of rigorous zero-Doppler geometry, i.e., with orthogonal t and τ (azimuth and range) annotation. The S-1 SAR processor applies a simple shift to modify the azimuth timing annotation [31], thereby leaving sub-pixel distortions and range dependent shifts of 2-4 m in the azimuth times of the S-1 products. The algorithm for the post-processing correction Δt_{BA} therefore determines both the inverse of the original azimuth shift and the rigorous correction for each correction grid point as [23]:

$$\Delta t_{BA} = \frac{\tau_{mid}}{2} + \frac{\tau_g}{2} - rank \cdot PRI, \tag{6}$$

with τ_{mid}, τ_g and PRI being the reconstructed mid-swath range time, the range time of the correction grid point, and the pulse repetition interval of the considered burst, respectively. The parameter $rank$ specifies the number of PRI events between transmitted pulse and return echo. All the required parameters are annotated in the S-1 SLC SAR product [50]. Because $rank$ and PRI change from sub-swath to sub-swath, the correction changes considerably across the swath, especially so with IW3, see Fig. 3.

5) Doppler-induced Range Shift Mitigation: The transmitted radar pulses experience frequency shifts from the Doppler effect caused by the satellite's motion. These shifts are usually ignored by SAR image processing, because the effect cancels almost completely for SAR modes with azimuth spectra close to zero-Doppler, e.g., stripmap SAR with zero-Doppler steering. However, for the Terrain Observation with Progressive Scan (TOPS) mode used by S-1, which generates data with large Doppler centroid variations across the bursts, the impact of the Doppler shift becomes significant, especially towards the edge of the bursts where the Doppler effect is the largest [23]. During spectral range compression the Doppler frequency leads to a proportional spatial shift of the compressed pulses. This is not handled by the S-1 SAR processor for the IW and EW data and the shifts ranging between $\pm 0.4\,\mathrm{m}$ across each burst have to be removed, see Fig. 3. The correction value

$$\Delta\tau_{DRS} = f_{DC,g}/K_r \tag{7}$$

is proportional to the Doppler centroid frequency $f_{DC,g}$ for the grid point location t_g, τ_g which has to consider the beam steering of the TOPS mode [23]. The K_r denotes the frequency modulation (FM)-rate of the range chirp annotated in the SAR products [50].

6) FM-rate Mismatch Azimuth Shift Mitigation: Focusing of the azimuth signal requires knowledge of the azimuth FM-rate which is driven by the sensor-to-ground geometry. The range-dependent change is modelled with sufficient detail when defining the matched filter. However, the effective velocity parameter underlying the azimuth FM-rate computation is kept constant during the processing of large azimuth blocks. These comprise up to several seconds in azimuth dimension, e.g., the 3 s burst size of S-1 TOPS. While for stripmap SAR with zero-Doppler steering, the effect of the mismatch (quadratic phase error, [1]) is mainly a defocussing of the image, there is also a shift in azimuth for TOPS products. Around the borders of mountainous areas, shifts of a few meters can be found at the edge of the burst because the average scene height assumed for the FM-rate calculation can differ from the local height by thousands of meters.

The azimuth FM-rate mismatch correction is computed from the annotated Doppler centroid frequency at the grid location $f_{DC,g}$ and the azimuth FM-rate k_a, g applied by the SAR processor. The correction is calculated by considering the difference to the true azimuth FM-rate $k_{a,geom}$ derived from the orbit to grid point geometry

$$\Delta t_{FMM} = f_{DC,g} \cdot \left(\frac{1}{-k_{a,g}} - \frac{1}{-k_{a,geom}} \right). \tag{8}$$

The computed corrections show strong variations across affected burst as well as spatial correlation with topographic features contained in the scene, see Fig. 3.

C. Product Usage

For the application of ETAD timing corrections, the NetCDF product has to be accessed and corrections have to be applied on burst level. In order to facilitate straightforward data usage, ESA maintains an API to extract burst timing corrections from the NetCDF file [51].

1) Application of ETAD Product to Correct SLC Data Timing: S-1 ETAD gridded corrections are applied to SLC data on a burst by burst basis, whose original pixel positions are defined by the annotated time coordinates (t, τ). The time annotated ETAD correction grids have first to be resampled to the higher resolution SLC raster by applying a simple bilinear interpolation. This can be performed for any combination of correction grids or most conveniently by using the prepared summation grids. The sum of ETAD range corrections $\Delta_\tau(t, \tau)$ and azimuth corrections $\Delta_t(t, \tau)$ is then subtracted from the original SLC slant range and azimuth timings, thus resulting in an irregularly gridded but timing corrected SLC dataset. Note, the bistatic azimuth correction (6) and the Doppler shift range correction (7) are annotated in the ETAD product as correction layers with opposite sign, and thus have to be subtracted from the SLC timing annotation as all the other corrections. In order to resample the corrected and

TABLE III
SUMMARY OF GEODETIC CALIBRATION SITES EQUIPPED WITH TRIHEDRAL CORNER REFLECTORS.

Calibration Site	**Site Location** (latitude/longitude)	**SAR Ground Infrastructure**	**Description**
Metsähovi Geodetic Observatory	Finland (60.2176 °/24.3945 °)	1.5 m CR (1)	CR facing East (S-1 descending tracks); Reference coordinates from terrestrial local tie survey ($< 5\,\mathrm{mm}$)
Wettzell Geodetic Observatory	Germany (49.1447 °/12.8783 °)	1.5 m CR (2)	CRs facing East and West (S-1 ascending and descending tracks); Reference coordinates from terrestrial local tie survey ($< 5\,\mathrm{mm}$)
Yarragadee Geodetic Observatory	Australia (-29.0474 °/115.3461 °)	1.5 m CR (2)	CRs facing East and West (S-1 ascending and descending tracks); Reference coordinates from terrestrial local tie survey ($< 10\,\mathrm{mm}$)

now irregularly spaced raster back to a regular grid, phase preserving complex interpolation has to be used [52], and subsequent processing can continue as normal. For a detailed description of timing corrections of individual targets and S-1 SLC data, the reader may refer to [33]. The application to S-1 GRD (Ground Range, Multi-look, Detected) products is also possible with some caveats, see [33], but in order to achieve high timing accuracies we always recommend to correct S-1 SLC data.

2) Application of ETAD Product to Correct Phase: Phase corrections should be calculated from the individual $\Delta\tau$ range corrections that are converted to radians. Let λ_{S1} be the wavelength of the sensor and c the speed of light in vacuum:

$$\begin{aligned}\Phi_{ETAD} = -\,(&\Delta\tau_{tro} + \Delta\tau_{tides} - \Delta\tau_{ion} + \ldots \\ &\Delta\tau_{cal} + \Delta\tau_{pol}) \cdot \frac{2\pi c}{\lambda_{S1}}.\end{aligned} \tag{9}$$

Note the inverse sign for ionospheric phase correction due to the dispersive properties of the ionosphere. The range calibration $\Delta\tau_{cal}$ and polarization calibration $\Delta\tau_{pol}$ given in the product annotation only have to be accounted for if interferograms are calculated from S-1A and S-1B combinations or from different polarization channels [33]. Currently, the only missing range correction that is annotated in the ETAD product, the Doppler range shift system correction (see section II-B5), is omitted from this formula as it is not clear to which extent its effect is already compensated in various interferometric processors.

III. VALIDATION AT GEODETIC CALIBRATION SITES

A. Sites and Methods

The quality and accuracy of ETAD timing corrections can be validated with S-1 measurements of stable calibration targets with known reference coordinates. For assessing the product, we used triangular trihedral corner reflectors (CRs) with 1.5 m edge length, which are installed at the geodetic stations of Metsähovi (Finland), Wettzell (Germany) and Yarragadee (Australia) [20], [53]. The procedures are well established and are commonly applied when determining the absolute location error (ALE) of SAR systems [21], [54], [55]. Such studies were also performed by DLR with S-1 data to verify the correction methods and more details on ALE assessment can be found in [23].

The ALE of a SAR system is determined by comparing reference values for range and azimuth computed from the known target position and the precise orbit solution with the range and azimuth target coordinates extracted at sub-pixel level from the SLC SAR images. The comparison has to account for the errors introduced by the atmosphere, the solid Earth deformations, and the SAR processing effects, which allows validation of the corrections offered by the ETAD products. For each SAR image and the corresponding ETAD product, residuals are computed and converted to units of meters as follows:

$$\begin{aligned}\Delta rg &= (\tau_{SAR} - \tau_{ref} - \Delta\tau_{ETAD,sum,rg}) \cdot c/2 \\ \Delta az &= (t_{SAR} - t_{ref} - \Delta t_{ETAD,sum,az}) \cdot v_{beam}\end{aligned} \tag{10}$$

where τ, t_{SAR} denote the target coordinates of the SAR image, τ, t_{ref} are the computed reference values, $\Delta\tau_{ETAD,sum,rg}$ and $\Delta t_{ETAD,sum,az}$ are the total sum of ETAD corrections in range and azimuth, respectively, c is the speed of light in vacuum and v_{beam} is the zero-Doppler beam velocity. The beam velocity of S-1 is in the order of 6800 m/s and is annotated in the ETAD product.

Because ETAD products provide the S-1 precise orbit along with all the corrections layers, the ALE processing becomes straightforward and consists only of the following steps:

1) *Point Target Analysis*: Extraction of the target range and azimuth coordinates from the S-1 SLC SAR image at sub-pixel level. A two-step procedure is applied. Spectral zero-padding is used to 32x oversample the complex image data around the peak, followed by the fit of an analytic elliptic paraboloid to define the peak position with a precision better than 1/1000th of a pixel [56].
2) *ETAD Product Evaluation*: Interpolation of the ETAD product range and azimuth summation layers (see section II-C1) for the obtained range and azimuth coordinate location.

TABLE IV
SUMMARY OF S-1 DATA AND ETAD PRODUCTS USED FOR VALIDATION AT THE CALIBRATION SITES.

Site / Pass	Sensor	Relative Orbit Nr.	Mode	Pol.	No. of Products	Remarks
Metsähovi / DESC 1	S-1A	51	IW	VV, VH	7	
Metsähovi / DESC 2	S-1B	153	IW	VV, VH	6	
Wettzell / ASC	S-1A	44	IW	VV, VH	8	CR located in burst overlap
Wettzell / DESC	S-1B	95	IW	VV, VH	7	CR located in burst overlap
Yarragadee / ASC	S-1B	25	SM	HH	18	
Yarragadee / DESC	S-1B	61	IW	VV, VH	8	CR located in swath overlap

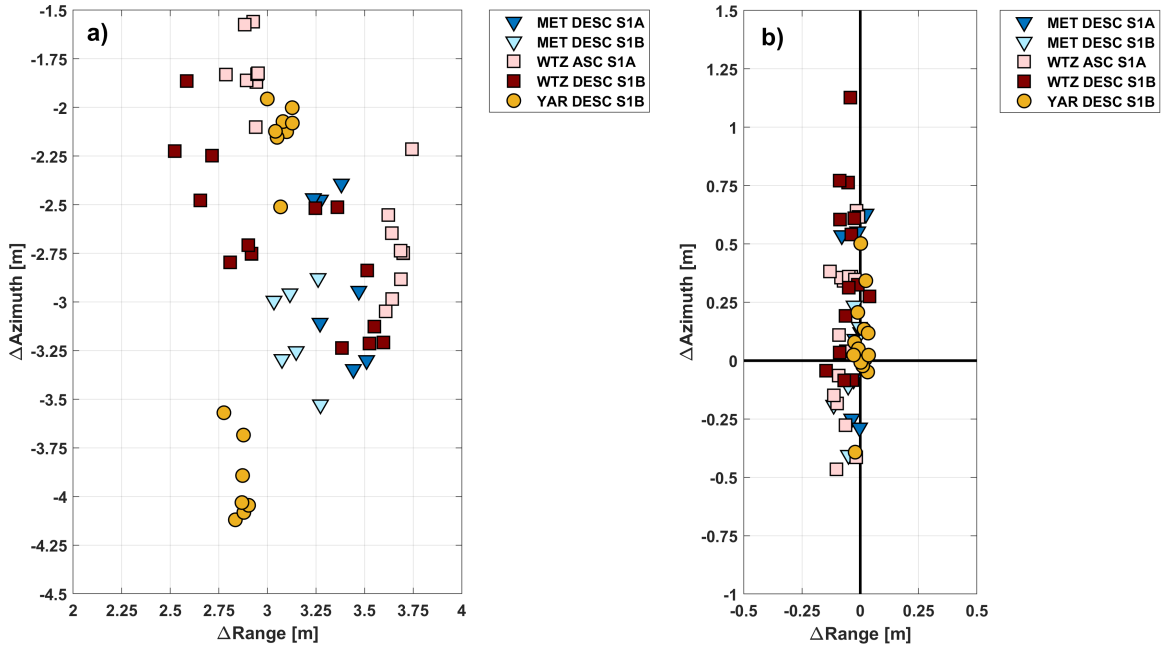

Fig. 4. Geolocation residuals obtained with S-1 IW data for the different test sites. Raw results without applying corrections (a) and results when applying the ETAD product (b). Note the different axis scaling.

3) *Reference Value Determination*: Computation of reference zero-Doppler range and azimuth coordinates from the precise orbit embedded in the ETAD product and the known ITRF reference coordinates of the target, using the SAR range-Doppler equations in zero-Doppler configuration (1)(2).
4) *ALE Analysis*: Comparison of extracted and computed range and azimuth coordinates, considering the corrections, see equation (10).

The procedure is performed individually for each S-1 SLC SAR and ETAD product, which yields sets of residuals for each calibration site and for both instruments S-1A and S-1B. The results can be analyzed with respect to:

- Standard deviations in range and azimuth (product precision, sensor noise)
- Remaining offsets in range and azimuth (product accuracy, sensor biases)
- Consistency of S-1A and S-1B when applying the ETAD product (S-1 system performance)
- Consistency of results regarding ascending and descending passes at the same site
- Performance of system corrections for CRs located in burst or swath overlap areas

The calibration sites hosting the trihedral CRs are described in Table III. Each of the geodetic observatories provides one or two permanently installed CR that are attached either to a deep concrete foundation or directly to stable bedrock. The sites have been measured with terrestrial geodetic surveys with a 3-D precision of better than 5 mm (Wettzell, Metsähovi) and better than 10 mm (Yarragadee). The coordinates were accurately transformed to the global ITRF 2014 at reference epoch 2010, applying the station's known local network to ITRF transformation parameters [57]. Test data for this validation activity consists of S-1 data acquired between August 2019 and August 2020 for which the ETAD products have been computed, see Table IV. The IW data covers a period of 3 months in summer 2019 to avoid any deterioration due to snow in the CRs. This yields 7-8 ETAD products per site and configuration, which have a temporal sampling of 12 days. SM data at Yarragadee was specifically acquired with a 24 days repeat interval for one year and all available products are used for the verification.

TABLE V
GEOLOCATION RESULTS (MEAN ± STANDARD DEVIATION) OBTAINED WITH IW DATA FOR THE DIFFERENT TEST SITES. ABSOLUTE LOCATION ERROR (ALE) WITHOUT APPLYING CORRECTIONS (RAW) AND AFTER APPLYING THE ETAD PRODUCT (ETAD).

Calibration Site & Sensor	**Range ALE [m]**		**Azimuth ALE [m]**	
	RAW	**ETAD**	**RAW**	**ETAD**
Metsähovi DESC S-1A	3.369 ± 0.110	-0.023 ± 0.032	-2.862 ± 0.412	0.170 ± 0.397
Metsähovi DESC S-1B	3.151 ± 0.098	-0.041 ± 0.042	-3.151 ± 0.249	-0.034 ± 0.243
Wettzell ASC S-1A	3.287 ± 0.394	-0.066 ± 0.038	-2.267 ± 0.522	0.125 ± 0.351
Wettzell DESC S-1B	3.092 ± 0.400	-0.054 ± 0.043	-2.695 ± 0.418	0.381 ± 0.369
Yarragadee DESC S-1B	2.968 ± 0.117	0.005 ± 0.021	-3.032 ± 0.951	0.064 ± 0.190
Total S-1A & S-1B	3.150 ± 0.320	-0.036 ± 0.045	-2.736 ± 0.687	0.159 ± 0.334

B. Geolocation Results for IW Products

Without applying any corrections, the ALE residuals of S-1 IW data show typical systematic effects which are caused by the different types of errors stemming from physical effects (atmosphere, solid Earth tides) and S-1 SAR system effects, see Fig 4a and RAW ALE results in Table V.

The range residuals are dominated by the approximately 3 m bias of tropospheric delay, as well as Doppler range shifts not corrected in the S-1 level 1 products, which are clearly visible in the results of the CRs situated in burst and beam overlaps: WTZ ASC, WTZ DESC, YAR DESC. Despite having been observed with the same atmospheric conditions, the residuals of these three calibration targets become divided into two groups that belong to the different overlapping bursts.

The azimuth ALE residuals are driven by the bistatic azimuth effects only partly compensated for in processed S-1 level 1 data [23], [58]. The impact is most prominent in the results of YAR DESC where the measurements are performed in overlapping beams (IW1, IW2). The azimuth results are separated by approximately 2 m because of the inter-beam bistatic biases. In summary, the uncorrected data yields a combined S-1 ALE result of $3.15 \pm 0.32\,\mathrm{m}$ in range and $-2.75 \pm 0.69\,\mathrm{m}$ in azimuth, see Table V. These findings are in perfect agreement with our earlier results obtained with S-1A and S-1B at the Australian CR array [23].

After applying the corrections from the ETAD product, the impact of the effects discussed above is greatly reduced. The range ALE offsets and standard deviations are now at a level of a few centimeters, showing only minor differences between different stacks, calibration sites, and S-1A and S-1B sensors (Table V, Fig. 4b). The azimuth ALE results show a similar improvement in eliminating the systematic discrepancies. However, after correcting all timing errors the geolocation precision becomes limited by the approximately 22 m azimuth resolution of the IW SLC data [31], which impacts measurement accuracy because of the signal to clutter ratio (SCR) of the used CRs. For the trihedral triangular CRs with 1.5 m edge length, the average SCR observed with the IW data is 22 dB, which translates into a theoretical azimuth precision ($1\,\sigma$) of 0.68 m when applying the error estimation assuming uncorrelated clutter [59]. In fact, our measurements are better than this prediction which may be caused by overestimated clutter or by correlated background clutter [60], but an overall SCR limitation is still manifested in the standard deviation of the azimuth residuals list in Table V. Nevertheless, the azimuth ALE of IW data benefits from the ETAD system corrections which enable comparable observations across the different test sites.

C. Geolocation Results for SM Products

With an average resolution of 2.5 m in range and 4.5 m in azimuth [31], the S-1 SM data has considerably higher azimuth resolution than IW data and therefore the attainable geolocation accuracy is higher as well because of the increase in target SCR and resolution. The uncorrected SM data shows an azimuth offset due to the bistatic error and a range offset mainly caused by the tropospheric delay, see Fig. 5a and RAW ALE results in Table VI. The additional spread in range is caused by the atmosphere and solid Earth tides.

Results for the corrected data are shown in Table VI and Fig. 5b. The corrections from the ETAD product remove the range bias and improve the range ALE standard deviation from 0.14 m to 0.02 m at the given test site. The range data becomes almost perfectly centered which confirms the consistency of the IW and SM range observations of S-1 when applying the ETAD corrections. In the ETAD product, the azimuth SM data is only corrected for the bistatic effect, which is mainly a bias, and the horizontal solid Earth tide deformations, which at the given site are at the $\pm 0.03\,\mathrm{m}$ level. Consequently, there is only a small improvement in the standard deviation, see Table VI, whereas the azimuth bias is largely removed.

Overall centering of the data is achieved with the ETAD timing calibration, which was determined for IW data (see section II-A). The results show that for range data the correction is already well defined, but for azimuth SM data there remains an offset of 0.15 m. Therefore, a refinement of the timing calibration auxiliary dataset used by the ETAD (see section II-B) has to be performed in order to adjust the SM geolocation accuracy in azimuth.

D. Discussion of Geolocation Results

The geolocation range results obtained with the ETAD product are well within the range correction specifications (see section II-A). The range accuracy achieved with IW data across all tests with different beams and sensors is better

TABLE VI
GEOLOCATION RESULTS (MEAN ± STANDARD DEVIATION) OBTAINED WITH SM DATA AT THE YARRAGADEE TEST SITE. ABSOLUTE LOCATION ERROR (ALE) WITHOUT APPLYING CORRECTIONS (RAW) AND AFTER APPLYING THE ETAD PRODUCT (ETAD).

Calibration Site & Sensor	Range ALE [m]		Azimuth ALE [m]	
	RAW	ETAD	RAW	ETAD
Yarragadee ASC S-1B	3.318 ± 0.142	0.011 ± 0.020	-2.093 ± 0.048	0.157 ± 0.046

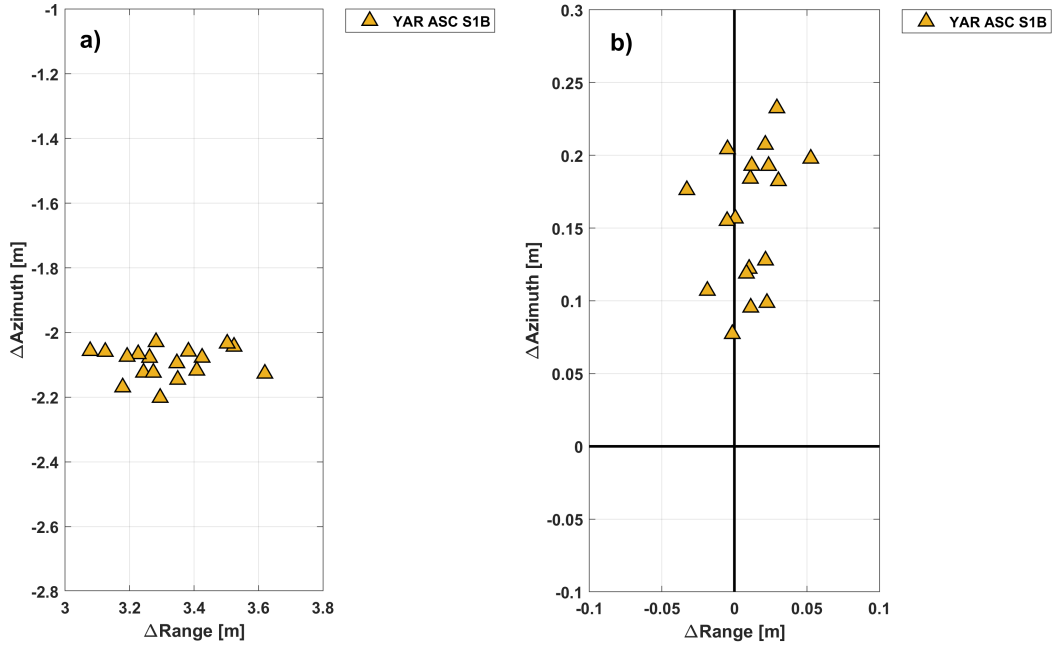

Fig. 5. Geolocation residuals obtained with S-1 SM data for the Yarragadee test site. Raw results without applying corrections (a) and results when applying the ETAD product (b). Note the different axis scaling.

than 0.05 m and even better (0.02 m) for SM range data. The azimuth geolocation, however, is limited by effects beyond the scope of the ETAD product. Whereas the results achieved with SM data show a very high geolocation precision of 0.05 m in azimuth that is clearly within ETAD specification, the geolocation precision obtained with IW data is 0.3 m due to the coarser azimuth resolution and the limited SCR of the CRs. We have no reason to assume that the ETAD azimuth corrections for IW are worse than those for SM. Moreover, both modes show a systematic azimuth offset of about 0.15 m.

These remaining errors are the combined effect of orbit accuracy, uncompensated sensor biases, and the impact of SCR versus resolution of the SAR image product:

- The accuracy of the S-1 precise orbit product is better than the required 5 cm 3-D RMS [13].
- For the processed IW data, the SCR of the CRs reads 22 dB which translates into a theoretical geolocation precision of $\pm 0.09\,\mathrm{m}$ (range) and $\pm 0.68\,\mathrm{m}$ (azimuth) when applying the average S-1 IW image resolution of 3 m (range) and 22 m (azimuth) [31], [59].
- For the processed SM data, the SCR of the CRs reads 28 dB which translates into a theoretical geolocation precision of $\pm 0.04\,\mathrm{m}$ (range) and $\pm 0.06\,\mathrm{m}$ (azimuth) when applying the average S-1 SM image resolution of 2.5 m (range) and 4 m (azimuth) [31], [59].
- The biases stem from S-1 sensor characteristics, system aging, and other unknown effects that have to be calibrated for the system.

Considering the impact of SCR, the ETAD products performs to specification and the accuracy can be ensured by refining the sensor timing calibration used by the ETAD processor, see the outlook in chapter VI. In summary, the performed ETAD product validation confirms that the product behaves as expected and the geometric accuracy attainable at global scale with S-1 data is now at least 0.2 m in range and 0.1 m in azimuth.

IV. ICE VELOCITY MONITORING IN GREENLAND

The ice flow of the Greenland ice sheet is routinely monitored by ENVEO through the Copernicus Climate Change Service (C3S) for Land Hydrology and Cryosphere [61]. In this operational framework, ice velocity (IV) is mapped by applying the well-established SAR OT technique to each 6-day and 12-day pair of S-1 SLCs acquired over Greenland [27].

The OT technique consists in determining the local misalignment between repeat pass SAR images by finding the maximum of the cross correlation peak that corresponds to the offset [24]–[26], [62]–[64]. When OT is applied to ice sheets or glaciers and if SAR images are geometrically coregistered beforehand, the estimated offsets can be assumed to be directly

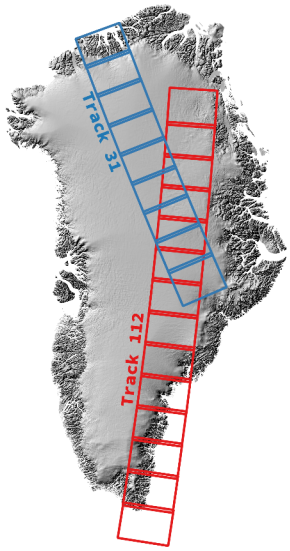

Fig. 6. Coverage of S-1 Greenland IV data: track 31 (blue), track 112 (red).

related to ice motion. In practice, amplitude-based OT uses SAR amplitude images as templates to determine displacements of ice surface features such as crevasses, rifts or edges. In case speckle is coherent it can provide even higher accuracy than features. OT estimates displacements in both the range and azimuth directions, that are subsequently normalized by the temporal baseline to obtain velocity measurements. One of the main error sources is uncompensated propagation delays, in particular the tropospheric and ionospheric ones, that are in turn misinterpreted as ice motion. In order to correct for such biases, OT results are usually calibrated against stable or slow-moving areas (e.g. rocks or ice divides) in a post-processing step. However, calibration can turn out to be challenging in regions lacking stable areas and in situ measurements, e.g. for tracks covering only the interior of the ice cap. In this case, ETAD products provide a valuable alternative. In this section, the use of timing delay corrections as provided by ETAD products is investigated for compensating biases in OT IV measurements.

A. Methods

In the case of OT, we consider two approaches to compensate timing delays by applying ETAD corrections: the first approach is the SLC timing correction of individual SAR images before processing, which is described in section II-C1; the second approach is a post-processing bias correction of local pixel shifts estimated between two SAR SLC images. The SLC timing correction is of interest if one has to process the same SLCs with multiple techniques; for processing a dataset with OT only, or for correcting archive results, the second method is faster and computationally less expensive. In both cases, the ETAD correction module can be easily integrated to standard processing chains.

As explained in section II-C1, the use of ETAD for correcting SLC timing enables to resample each pixel to its accurate position in the SAR image by correcting timing errors of various origins. The ETAD SLC timing correction must be applied to both the reference and secondary SLCs used for OT. The output products are timing-corrected SLCs, directly ingested into the standard OT processing chain. This method is expensive because the resampling has to be performed on complex images at full resolution on aliased TOPS data, i.e. at non-zero-Doppler frequencies. The interpolator must be capable to handle very small shifts of less than 1/100 of a pixel. Moreover, it doubles the storage space of the SLC data, which can become critical for wide-scale monitoring. The second approach requires no interpolation of SLC data as it applies the corrections directly on the shift vectors derived from OT.

Let us consider that the offset-tracking range and azimuth velocity estimates v_{rg}^{OT} and v_{az}^{OT} are already available for a given pair of uncorrected reference and secondary SLC. Then the post-processing bias correction consists of: 1) upscaling the reference and secondary ETAD timing delays to the SLC grid multilooked at the OT grid resolution using a bilinear resampling, 2) resampling the secondary ETAD to the reference OT geometry, and 3) correcting the offset tracking velocity estimates according to:

$$v_{rg}^{OT'} = v_{rg}^{OT} - \frac{\left(\Delta\tau_{ETAD,sum,rg}^{ref} - \Delta\tau_{ETAD,sum,rg}^{sec,res}\right)}{\Delta T} \cdot \frac{c}{2} \tag{11}$$

$$v_{az}^{OT'} = v_{az}^{OT} - \frac{\left(\Delta t_{ETAD,sum,az}^{ref} - \Delta t_{ETAD,sum,az}^{sec,res}\right)}{\Delta T} \cdot v_{beam} \tag{12}$$

where $v_{rg}^{OT'}$ and $v_{az}^{OT'}$ are the corrected OT velocity estimates in the range and azimuth directions, respectively, ΔT is the temporal baseline between the reference and secondary acquisitions, $\Delta\tau_{ETAD,sum,rg}^{ref}$ and $\Delta\tau_{ETAD,sum,az}^{ref}$ are the upscaled sums of ETAD range and azimuth timing corrections corresponding to the reference acquisition, $\Delta\tau_{ETAD,sum,rg}^{sec,res}$ and $\Delta\tau_{ETAD,sum,az}^{sec,res}$ are the upscaled and resampled sums of ETAD range and azimuth timing corrections corresponding to the secondary acquisition, c is the speed of light and v_{beam} is the zero-Doppler beam velocity. This calculation is performed pixel-wise and the position indices have been omitted for the sake of readability.

The post-processing ETAD correction is operated at multilooked resolution and has therefore reduced computational and storage costs compared to the SLC timing correction. It also opens the possibility to correct archive results without the need of a full reprocessing. The SLC timing corrections are still worth considering in the case of multi-approaches studies. Both approaches are evaluated in the following using the dataset described below.

B. Dataset and Processing

For testing the OT IV bias compensation, the two methods are tested on a dataset of S-1 SLCs acquired over Greenland. ETAD products have been computed for each acquisition of the dataset described in Table VII. The dataset consists of long stripes of S-1 IW SLC data acquired along ascending

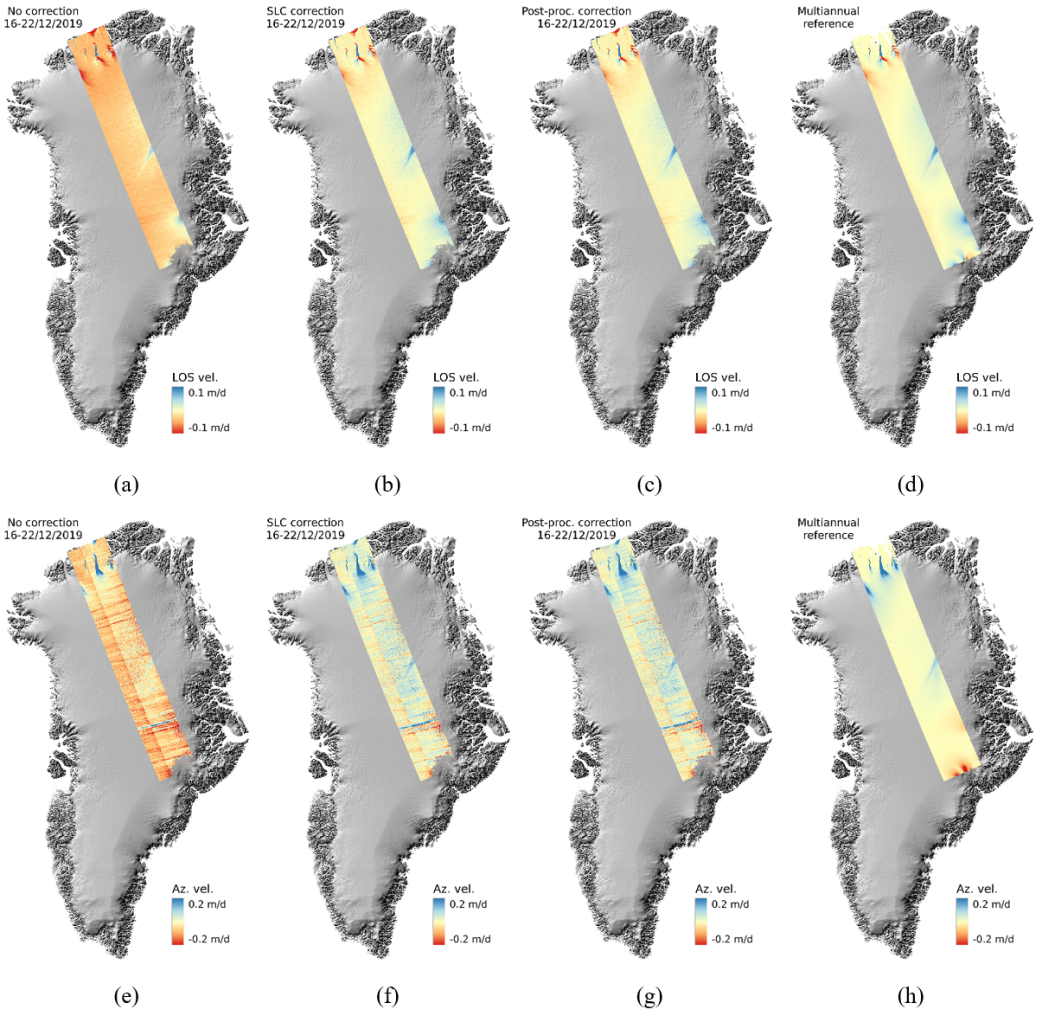

Fig. 7. Range (a-d) and azimuth (e-h) velocity components measured with (a, e) uncorrected OT, (b, f) OT with SLC timing corrections, (c, g) OT with post-processing corrections and compared to (d, h) the multiannual velocity reference. OT is applied to a 6-day S-1A and S-1B pair acquired along track 31 (16/12/2019-22/12/2019).

TABLE VII
DESCRIPTION OF SENTINEL-1 DATASET USED FOR THE GREENLAND EXPERIMENT.

Pass	Sensor	Relative Orbit Nr.	Mode	Pol.	Products
ASC	S-1A	31	IW	HH	16/12/2019
					28/12/2019
ASC	S-1B	31	IW	HH	22/12/2019
DESC	S-1B	112	IW	HH	16/12/2019
					28/12/2019

and descending tracks with 6- and 12-day repeat during winter 2019. These tracks cover at the same time fast ice streams, the slow-moving ice sheet interior and stable rocks on the coast, see Fig. 6. The tracks, the coverage and the repeat interval (6 and 12 days) are representative of the operational scenario used in the C3S IV monitoring service [61].

For each possible pair of acquisitions, OT is applied without bias compensation, with ETAD SLC timing corrections, and with ETAD post-processing corrections. Range and azimuth velocities are calculated on a grid multilooked on 40×20 pixels in the range and azimuth directions respectively, filtered and eventually geocoded on a 100 m grid with polar stereographic projection. Measurements with a cross-correlation below 0.1 are dismissed. Processing parameters are kept constant for all methods. For validation, the results are compared with a multiannual reference IV map generated with OT. The reference map is the solution of a least-squares problem made up of more than 5 years of S-1 OT measurements, each individual 6- and 12-day OT results being calibrated against stable and slow-moving areas. This reference map is hence representative of the stable state of the Greenland ice sheet. During winter, little ice flow variations are expected and OT IV measurements should hence be as close as possible to this reference.

C. Results and Discussion

The performance of ETAD corrections can be qualitatively appreciated by comparing the multiannual IV reference to the OT IV results without bias compensation, with the ETAD

TABLE VIII
DESCRIPTION OF SENTINEL-1 DATASET USED FOR THE GREENLAND EXPERIMENT.

S-1 pair	Orbit Nr.	ΔT (days)	Spatial average of LOS velocity residuals (m/day)			Spatial average of azimuth velocity residuals (m/day)		
			No correction	SLC correction	Post-proc. correction	No correction	SLC correction	Post-proc. correction
16/12/2019 - 22/12/2019	31	6	0.036 ± 0.008	0.002 ± 0.008	0.002 ± 0.008	0.063 ± 0.057	-0.009 ± 0.057	-0.012 ± 0.057
22/12/2019 - 28/12/2019	31	6	-0.025 ± 0.007	-0.001 ± 0.007	-0.001 ± 0.007	0.069 ± 0.048	0.004 ± 0.048	0.006 ± 0.048
16/12/2019 - 28/12/2019	31	12	0.005 ± 0.007	0.001 ± 0.007	0.001 ± 0.007	-0.001 ± 0.031	-0.001 ± 0.031	-0.001 ± 0.031
16/12/2019 - 28/12/2019	112	12	-0.004 ± 0.093	-0.006 ± 0.091	-0.006 ± 0.093	-0.001 ± 0.170	-0.003 ± 0.168	-0.003 ± 0.170

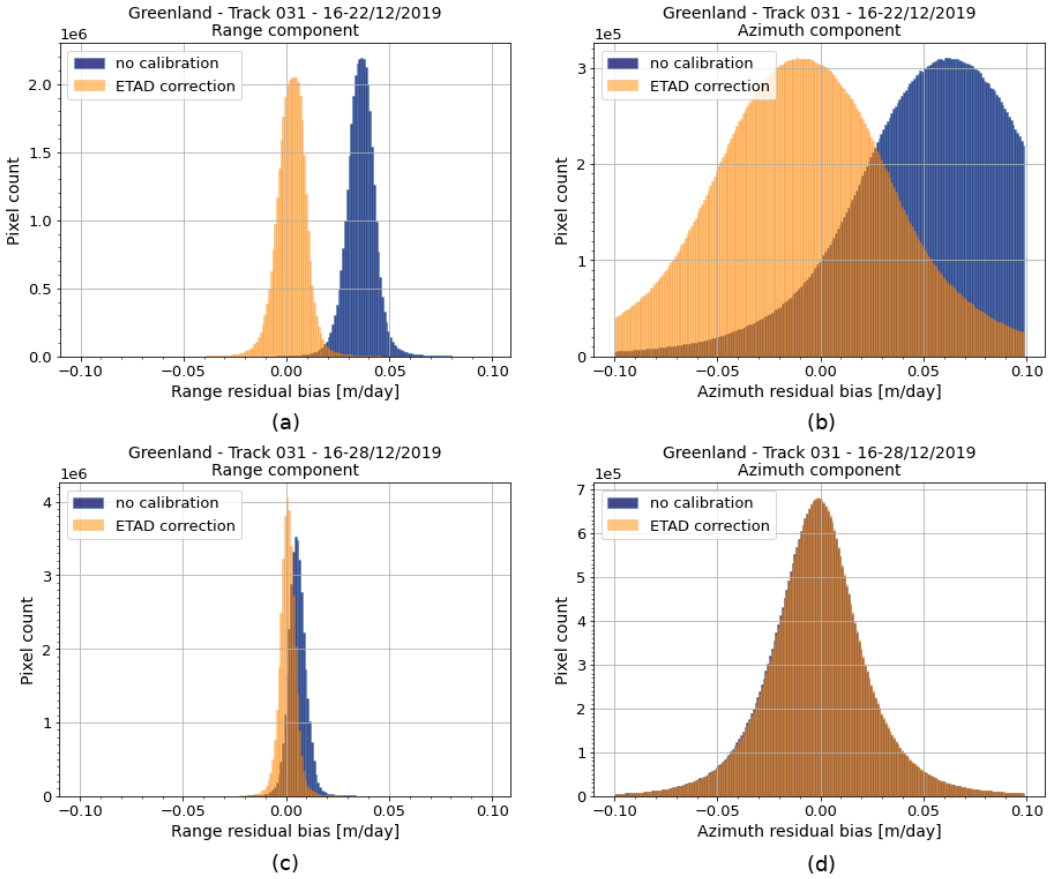

Fig. 8. Histogram of range and azimuth OT velocity residuals for 6- and 12-day pairs (track 31), with (orange) and without (blue) ETAD SLC timing corrections. Residuals are computed as the difference of the OT results compared to the multiannual velocity reference. (a) 16/12/2019-22/12/2019 - range velocity residuals. (b) 16/12/2019-22/12/2019 - azimuth velocity residuals. (c) 16/12/2019-28/12/2019 - range velocity residuals. (d) 16/12/2019-28/12/2019 - azimuth velocity residuals.

SLC timing correction, and with the ETAD post-processing correction, as shown in Fig. 7 for a 6-day pair involving S-1A and S-1B. The uncorrected velocities show an obvious error for the range and azimuth components when compared to the reference solution. In particular, the velocity differs from zero on the coast, where the rocks are free of ice and non-moving. In addition to the large-scale error, the azimuth component also suffers from local ionospheric streaks. Ionospheric streaks are shifts in the azimuth position caused by kilometer-scale disturbance of the ionosphere electron content [65]. They are commonly observed for OT processing in the polar regions and remain challenging to correct. Both the ETAD

SLC timing correction and the ETAD post-processing bias correction efficiently remove undesired large-scale trends and inter-sensor biases, showing velocity estimates close to zero on rocky areas. However, due to the coarser natural resolution of the underlying ionospheric data compared to the scale of such local ionospheric disturbances, and the omission of ionospheric corrections for azimuth timings in ETAD products (see sectionII-B2), the streaks remain uncorrected for the azimuth component.

For assessing quantitatively the performance of the correction approaches, we compute the difference between the reference velocity and the OT measurements for each pair and each method. This deviation with respect to the reference velocity is referred to as the velocity residual and is calculated pixel-wise for the range and azimuth components. A typical distribution of these residuals with and without ETAD corrections is shown in Fig. 8 for a 6-day pair and a 12-day pair. The ETAD post-processing corrections yield results practically identical to the SLC timing corrections, and are hence not displayed in this figure. Both the range and azimuth components appear to be normally distributed. Residuals of the azimuth components have a larger spread than those of the range components, due to the ionospheric streaks introducing local errors that cannot be corrected with ETAD. In the 6-day case, the residuals of the uncorrected OT results are distributed around a non-zero center value for the range and azimuth components (about 0.035 m/day and 0.065 m/day, respectively). Applying the SLC timing corrections, the distribution is shifted towards zero and the bias is significantly reduced to approximately 0.002 m/day and 0.01 m/day in range and azimuth, respectively.

However, for the 12-day example, the bias is smaller and the improvement is therefore less significant. For the range component, the distribution is still shifted by about 0.004 m/day towards zero, but for the azimuth component, the shift is smaller than 1 mm/day and the uncorrected and corrected residual distributions overlap. The reduced improvement in the 12-day case is expected as the OT measurements are usually less biased for longer temporal baseline, because: 1) OT has a better sensitivity to large displacements; 2) the displacements measured with OT are normalized by the temporal baseline to calculate velocities and the contribution of the path delay therefore decreases as the temporal baseline increases, making 12-day pairs less affected by timing errors than 6-day pairs. The scaling by the temporal baseline should in theory yield an accuracy of 12-day OT results better than the 6-day case by a factor 2, although a larger amount of scenes would be necessary to prove it.

For all the four analyzed pairs and both the corrections methods, the average residual values and their standard deviations are listed in Table VIII. As already observed with the histograms, for 6-day pairs, the average residual bias improves from a few centimeters per day in the uncorrected case to less than 1 cm/day with the ETAD, and even better in some cases. The standard deviation remains mostly unchanged when the ETAD corrections are applied. The small residuals obtained when the ETAD corrections are applied highlight the reduced need for velocity calibration that is required in the uncorrected case. Furthermore, the improvement is similar for the SLC timing corrections and the post-processing bias corrections, both methods being therefore considered equivalent.

Due to the bias being smaller in the 12-day case, the improvement provided by the ETAD correction is strongly reduced. The particular pair over track 112 even shows slightly worsened measurements when ETAD corrections are applied. The performance of ETAD correction in this particular example must however be put in perspective, considering that 1) track 112 crosses a region of high accumulation located on the southeastern coast of Greenland, where correlation is reduced and errors might be introduced, while the situation might be improved locally in some other places; 2) the mean correction and the mean residual velocity are subcentimetric, which is at the edge of OT noise floor and thus making variations of the residuals between the uncorrected and corrected cases of little significance [24], [59]. Furthermore, the combination of high accumulation, causing inaccuracies in the velocity measurements, associated to a wide variety of velocities in the scene leads to overall larger standard deviations of the residuals compared to the other examples.

V. InSAR Applications in Norway

The most significant noise source in InSAR time series analysis is the spatially varying and strongly time dependent delay through the atmosphere, see for instance [66], [67]. The atmospheric phase screen (APS) present in interferograms consists of a topography dependent part, and a topography independent part [68]. It has been demonstrated that the topography dependent component of the atmospheric phase screen may be reasonably predicted under certain conditions using only SAR data [69], or using auxiliary numerical weather models [70]. The topography independent part can be further decomposed into a relatively stable part over long spatial scales ($> 50\,\mathrm{km}$), and a part due to turbulent mixing with shorter spatial and temporal scales [7]. While the turbulent part of the atmospheric signal is not easily predictable, the components of spatial scales larger than about $50\,\mathrm{km}$ are typically captured well by NWMs.

A. Benefit of ETAD for InSAR

It is challenging to compensate for the APS present in SAR data [68]. Most mitigation approaches rely on assumptions about the statistical behavior of APS in space and time [66]. In particular, the APS is assumed to be smooth in the spatial domain, and decorrelated from acquisition to acquisition in the temporal domain. The latter assumption allows robust mitigation of the APS component due to turbulent mixing in a purely data driven manner. However, such methods like persistent scatterer interferometry or differential InSAR, e.g. [71], [72], usually perform well only on spatial scales up to a few tens of kilometers [73].

The long spatial scales and the topography dependent components are often still partially present after data driven APS mitigation. This typically happens in areas with complex topography, since the statistical assumption used in the estimation of APS is not entirely accurate. While purely data driven mitigation methods do exist, any reliable and operationally

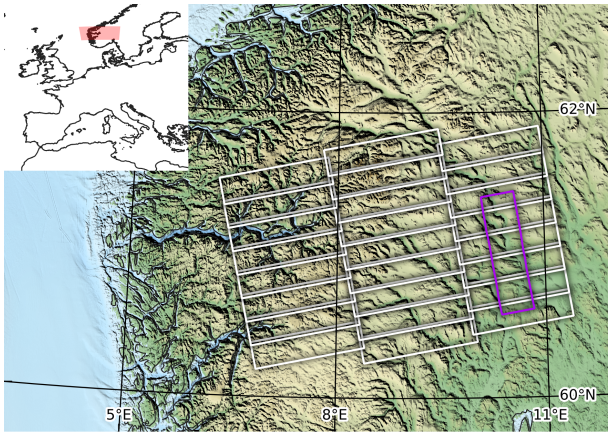

Fig. 9. Overview of AOI for InSAR study with "valley sub-AOI" indicated.

available a priori information that can support mitigation of the non-turbulent components is very valuable. Note that due to the turbulent components of the APS, ETAD is a supplement to data driven mitigation, not a replacement.

The ETAD product contains a dedicated layer, based on numerical weather models (Section II-B), for compensation of the atmosphere in S-1 SAR data. In this case study, effectiveness of the ETAD product for mitigation of non-turbulent APS components is evaluated.

B. Site: Norwegian fjords and mountains

Several studies [7], [74] have demonstrated the potential of NWM data for robust mitigation of non-turbulent APS components under favorable conditions. In this case study, the performance of such an approach is evaluated in a very challenging area in Southern Norway. The area is characterized by fjords, deep valleys, and complex topography in general. On the other hand, the amount of water vapor in the troposphere is relatively limited, potentially allowing reliable modeling of atmospheric effects. Figure 9 shows the location of the test area, and the outline of the available ETAD products for S-1 ascending track 44. Due to long periods of seasonal snow cover in Scandinavian mountains, only data between June and October are useful for InSAR analysis in this area. For this case study, ETAD products for a stack of 12 S-1 slices from the period Jul 2 to Sep 6, 2019, and involving S-1A and S-1B were used.

For qualitative evaluation of the performance of the stratification correction provided by ETAD, the area of interest is further restricted to a single long and relatively deep valley in the south-eastern part of the dataset. The valley Gudbrandsdalen is about 230 km long, and it is typically 10 km wide and 500-800 m deep in the narrower parts, where the stratification is most pronounced. The area of interest covers the southern half of the valley. The reduced area of interest is also indicated in Fig. 9.

C. Data Processing

Quantitative and qualitative performance analysis of the ETAD layers for the interferometric time-series applications was approached as follows:

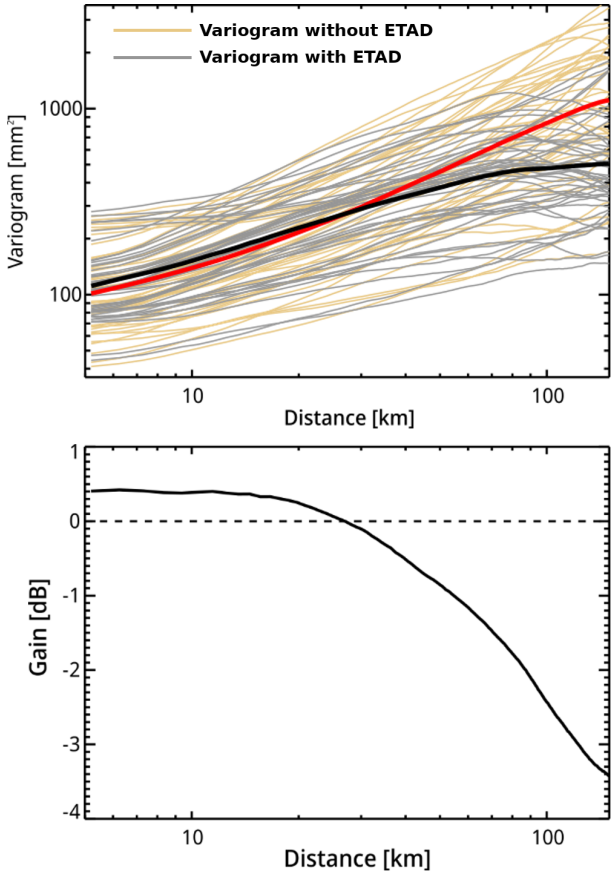

Fig. 10. Top: Variograms of interferometric phase before and after ETAD based correction for the 66 interferograms of the Norway test site. The thick red and black lines show the average variogram before and after correction, respectively. Bottom: The ratio of variograms before Γ and after Γ_{etad} correction, in dB as function of distance, gain $= 10log_{10}\left(\Gamma_{etad}/\Gamma\right)$.

1) Generate stack of differential Sentinel-1 IW mode burst interferograms, all 66 possible combinations.
2) Multilook the stack of interferograms to approximately the resolution of ETAD products (51 $\times$ 15 looks)
3) Mosaic burst interferograms to full slice interferograms
4) Unwrap interferograms
5) Calculate differential range delay correction, equation (9), from ETAD and resample to the interferogram grid.
6) Compensate unwrapped interferograms by applying ETAD correction and convert to units of range delay in millimeters.

Steps 1-4 are standard Differential InSAR processing steps for the stacks of S-1 data, resulting in 66 unwrapped interferograms for the given stack, and the ETAD correction is generated and applied in Steps 5 and 6. An example for the performed processing is shown in Fig. 11.

D. Results and Discussion

To evaluate the performance of the ETAD corrections for compensation of the long spatial scale components of the APS, we apply a variogram analysis to all available interferograms before and after the correction, similar to [74].

Figure 10 shows the results of the performed variogram analysis of all the 66 interferograms. The gain profile in the lower panel shows that the spatial variance drops significantly for scales larger than 25 km, indicating that the ETAD corrections in general effectively removed the APS on long spatial scales. On the other hand, a slight average performance loss ($\sim 10\,\%$) can be observed for spatial scales shorter than 25 km. This could be caused by the limited 200 m resolution of the ETAD product, which may lead to non-optimal corrections in mountainous terrain. A future ETAD product with add-ons for phase corrections in mountains could improve this significantly. Given the typical magnitude of the non-predictable turbulent mixing component in this challenging area, this is expected and not critical since straightforward data driven APS mitigation methods perform well on these spatial scales.

It is important to note that the variogram gain shown in Fig. 10, lower panel, is a relative measure, and thus only a relevant measure of success in cases where long spatial scale components and/or stratification are present in the uncorrected interferograms. For interferograms completely dominated by turbulent components, the gain profile will typically be relatively flat and slightly positive, i.e., the errors of the NWM would add to the atmospheric phase screen.

In summary, we observe a 3 dB improvement in precision at 100 km distances. While for example, with a simple data stacking approach, 4 independent interferograms would be required to achieve the same level of improvement, i.e. a factor of 2 lower standard deviation. Therefore, it can be stated that the ETAD correction may allow for faster detection of transient deformation because less temporal averaging is required.

E. Stratification considerations

The stratification influences the variogram at a broad range of spatial scales, and any potential improvement should theoretically be quantifiable. For this particular study, the stratification is not significantly affecting more than a small percentage of the total area of interest, leading to a smear effect that makes it hard to quantify the effect of ETAD based stratification correction in isolation. Thus, an overall variogram analysis of the whole area is not a suitable method for a direct quantitative analysis of stratification correction.

Nevertheless, some insight in the effect of ETAD corrections can be obtained by reducing the analyzed area to valleys where the stratification effect is dominant. The analyzed area is marked in Fig. 9. We inverted the stack of unwrapped interferograms of the reduced area with respect to a temporal reference and a high-coherence reference point (i.e., straightforward short baseline subsets-like inversion, see e.g. [72]). The result is a single-reference stack of 11 differential interferograms, each representing the phase difference between the first scene and each of the other scenes. By assuming that no significant motion happened during the 66-day time series and ignoring other noise terms, we may interpret these interferograms as APS only.

By comparing the inverted stack before and after ETAD correction, the effect on the stratification can be visually inspected. Figure 12 shows two examples. The first example is the typical case, where no residual stratification can be identified by visual inspection after the correction. The second example is the only example in this stack where the correction was suboptimal, and a barely visible residual stratification component is still present in the upper part of the corrected interferogram.

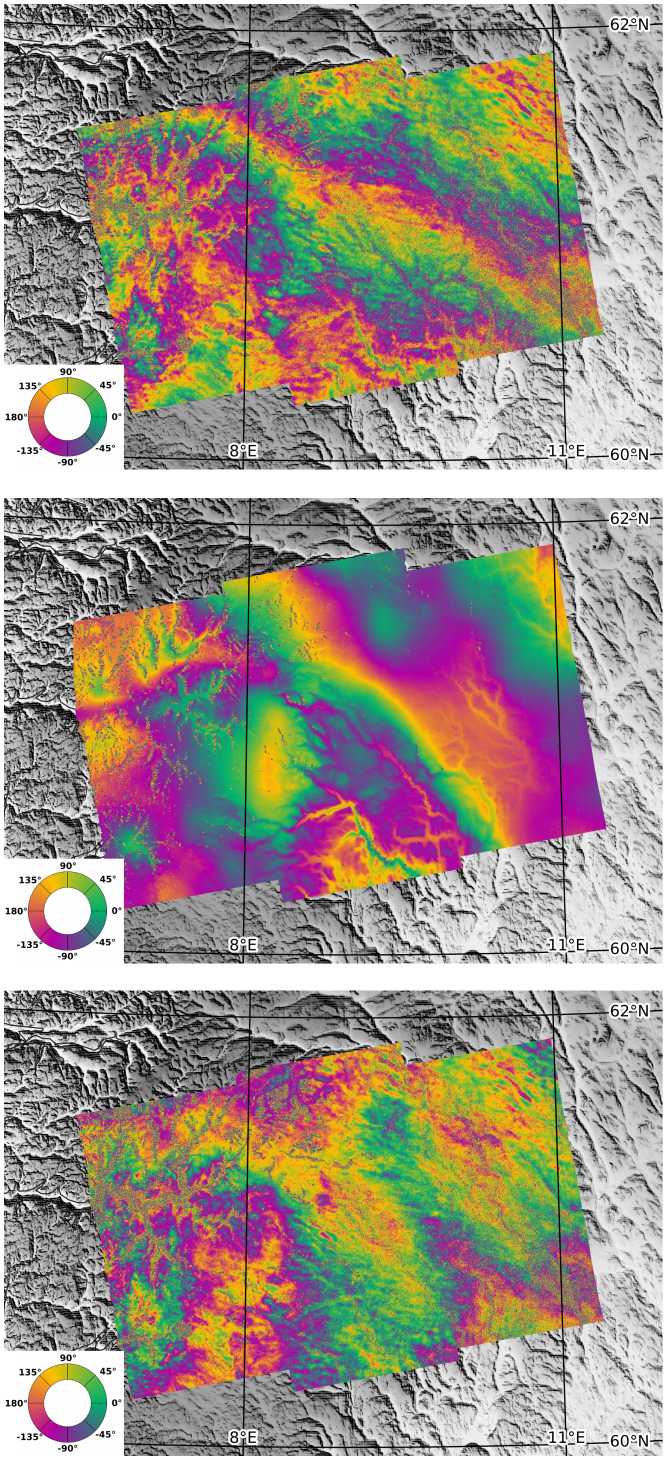

Fig. 11. Example illustrating the effect of ETAD correction, particularly the long wavelength component and stratification: (top) original interferogram, (middle) ETAD correction, (bottom) corrected interferogram. One color cycle corresponds to half a wavelength change in slant range, about 28 mm.

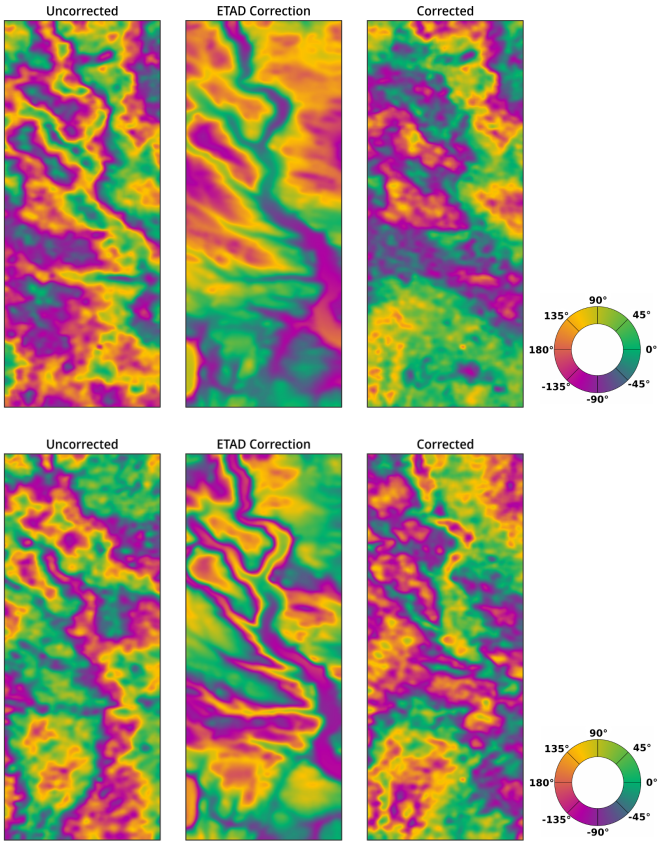

Fig. 12. Top: Interferogram July 2, 2019 vs August 7, 2019; illustrative (typical) example, stratification successfully mitigated. Bottom: Interferogram July 2, 2019 vs July 26, 2019 - the only example of slightly suboptimal ETAD correction in the stack. One color cycle corresponds to half a wavelength change in slant range, about 28 mm. Results display subset as marked in Fig. 9.

VI. Conclusions and Outlook

In this paper we outlined the ETAD product for S-1 SLC SAR images, presented the validation at geodetic calibration sites, and evaluated first applications to assess and demonstrate product usability. Product structure, the underlying algorithms, and its usage were discussed and examples are shown to emphasize the need for such timing corrections in SAR applications. The product comprises the corrections for tropospheric delay, ionospheric delay, solid Earth tides displacement, as well as the SAR processor effects of bistatic azimuth shifts, Doppler shifts in range, and azimuth shifts due to azimuth FM-rate mismatch, which in total can amount to several meters in range and azimuth, respectively.

The product was verified in dedicated geolocation experiments with accurately surveyed CRs and evaluated in two well-established SAR applications: ice velocity monitoring with OT and ground motion mapping with interferometry. The geolocation assessment performed at test sites in Australia, Finland and Germany confirms that the ETAD corrections meet the formal 1 sigma specification of $\pm 0.20\,\mathrm{m}$ in range and $\pm 0.10\,\mathrm{m}$ in azimuth. In general, we obtained experimental ALE results of better than 0.05 m. The result of 0.33 m obtained for the IW azimuth data is a consequence of the SAR image resolution and not of the ETAD product. Moreover, a bias of 0.15 m was found in the azimuth geolocation results of SM data and has to be addressed by an update of S-1A and S-1B sensor timing calibration used in the ETAD. From these results, we conclude that the high geolocation accuracy, which is attainable with S-1 data [23], [36], is now operationally accessible at a global scale.

For OT IV monitoring, ETAD products constitute an opportunity to get free from the need of stable calibration areas for bias correction, which are not always available in the acquired scenes. In the Greenland study case, two approaches have been tested for correcting biases with ETAD products: the a priori timing correction of SLCs and the post-processing correction of OT results. Both methods are easily integrated as optional modules in standard processing chains. It has been demonstrated with practical examples that both approaches yield similar performances. With both methods, long-scale trends are removed and the residual velocity biases are reduced down to subcentimetric values, which is about the limit of the performance expected for offset-tracking. The improvement is particularly significant for 6-day pairs that are more affected by timing delays than 12-day pairs. For operational IV monitoring, our recommendation goes towards the post-processing corrections, that involve less computational cost and less storage memory, and enable the reprocessing of archive results.

In the Norway case study, we have tested the performance of ETAD corrections for InSAR time series applications. A variogram analysis of all interferograms before and after ETAD correction showed that atmospheric phase components of spatial scales larger than 25 km are effectively mitigated. A visual inspection of the interferograms before and after correction indicates that also the atmospheric stratification is mitigated very well by ETAD in almost all cases. Although the analysis presented here shows a clear potential for operational utilization of ETAD, it should be noted that due to the presence of significant (unpredictable) turbulent atmosphere in this particular area, more data from multiple summer seasons are needed in order to quantitatively evaluate the performance effect for the stratification component. Moreover, the ionospheric layer provided with the ETAD product is targeting large scale pixel localization errors, whereas for interferometry the split-spectrum methods as described in [75] could be combined with ETAD to compensate for the high frequency ionospheric variations. Further verification and refinement of the presented approach with more data and at other locations worldwide would comprise a logical subject for future work.

At the time of writing (autumn 2021), activities for the integration of the SETAP software into the S-1 ground segment are ongoing. According to the current plans, pre-operations (not open to user) are set to start by the last quarter of 2021. Sustaining the ETAD production as part of S-1 routine operations, i.e., routine generation of the product in line with the SAR image products, will then be contemplated on the basis of an assessment of the pre-operational production. Additionally, ESA is currently supporting the hosting of SETAP in the Geohazards Exploitation Platform (GEP) in order to promote the early usage of the ETAD product from expert users of different application domains and gather valuable

feedback from the community [76]. After the product is brought into operations, and assuming a positive response from the community, ESA will evaluate possible alternatives to make ETAD products available also for historical S-1A and S-1B data.

Future maintenance of the processor and ETAD product quality is foreseen by the S-1 mission performance cluster that is responsible for calibration, validation, quality control, and end-to-end system performance assessment of all S-1 products [36]. This will also involve the maintenance of the SETAP auxiliary data files such as the timing calibration, which has to be refined for the SM azimuth data. Once the product has become fully integrated into regular operations, the accuracy gain using ETAD data can greatly simplify the processing steps in SAR applications, e.g., by making tie-points obsolete, and it will significantly improve the quality of displacement estimation with OT and InSAR methods.

ACKNOWLEDGMENT

We would like to thank the European Commission for funding this activity through the Copernicus Programme and ESA for supporting it with the S-1 ETAD project, ESA contract 4000126567/19/I-BG. The authors also thank all the colleagues from DLR and ESA who contributed to this project, as well as ENVEO and PPO.labs for feedback and performing first pilot studies with ETAD products. Finally, we thank the anonymous reviewers who provided valuable comments to improve the manuscript. The views expressed herein can in no way be taken to reflect the official opinion of the European Space Agency or the European Union.

REFERENCES

[1] J. Curlander and R. McDonough, *Synthetic Aperture Radar: Systems and Signal Processing*. John Wiley & Sons, Inc, 1991.

[2] I. G. Cumming and F. H. Wong, *Digital Processing of Synthetic Aperture Radar Data*. Artech House, 2005.

[3] M. Eineder, "Ocillator Clock Drift Compensation in Bistatic Interferometric SAR ," in *Proc. of IGARSS 2003 Conf., July 21–25, Toulouse, France*, 2003.

[4] G. Krieger and M. Younis, "Impact of oscillator noise in bistatic and multistatic SAR," *IEEE Geosci. and Remote Sens. Letters*, vol. 3, no. 3, pp. 424–428, 2006.

[5] T. Hobiger, R. Ichikawa, Y. Koyama, and T. Kondo, "Fast and accurate ray-tracing algorithms for real-time space geodetic applications using numerical weather models," *J. of Geophys. Res.*, vol. 113, pp. 1–14, 2008.

[6] G. Möller, R. Weber, and J. Böhm, "Improved Troposphere Blind Models Based on Numerical Weather Data," *NAVIGATION*, vol. 61, no. 3, pp. 203–211, 2014.

[7] X. Cong, U. Balss, F. Rodriguez Gonzalez, and M. Eineder, "Mitigation of Tropospheric Delay in SAR and InSAR Using NWP Data: Its Validation and Application Examples," *Remote Sens.*, vol. 10, no. 1515, pp. 1–21, 2018.

[8] C. Yu, Z. Li, and G. Blewitt, "Global Comparisons of ERA5 and the Operational HRES Tropospheric Delay and Water Vapor Products With GPS and MODIS," *Earth and Space Sci.*, vol. 8, no. 5, pp. 1–18, 2021.

[9] M. Hernández-Pajares, J. Juan, J. Sanz, R. Orus, A. Garcia-Rigo, J. Feltens, A. Komjathy, S. Schaer, and A. Krankowski, "The IGS VTEC maps: a reliable source of ionospheric information since 1998," *J. of Geod.*, vol. 83, no. 3-4, p. 263, 2009.

[10] M. Hernández-Pajares, J. Juan, J. Sanz, À. Aragón-Àngel, A. García-Rigo, D. Salazar, and M. Escudero, "The ionosphere: effects, GPS modeling and the benefits for space geodetic techniques," *J. of Geodesy*, vol. 85, pp. 887–907, 2011.

[11] J. Böhm and H. Schuh, Eds., *Atmospheric Effects in Space Geodesy*. Springer-Verlag Berlin Heidelberg, 2013.

[12] F. Massmann, K. Neumayer, J. Raimondo, K. Enninghorst, and L. H., "Quality of the D-PAF ERS Orbits before and after the Inclusion of PRARE Data," in *Proc. of 3rd ERS Symposium, 1997, Florence, Italy*, 1997.

[13] H. Peter, A. Jäggi, J. Fernández, D. Escobar, F. Ayuga, D. Arnold, M. Wermuth, S. Hackel, M. Otten, W. Simons, P. Visser, U. Hugentobler, and P. Féménias, "Sentinel-1A - First precise orbit determination results," *Advances in Space Res.*, vol. 60, no. 5, pp. 879–892, 2017.

[14] O. Montenbruck, S. Hackel, and A. Jäggi, "Precise orbit determination of the Sentinel-3A altimetry satellite using ambiguity-fixed GPS carrier phase observations," *J. of Geodesy*, vol. 92, pp. 711–726, 2018.

[15] S. Hackel, C. Gisinger, U. Balss, M. Wermuth, and O. Montenbruck, "Long-Term Validation of TerraSAR-X and TanDEM-X Orbit Solutions with Laser and Radar Measurements," *Remote Sens.*, vol. 10, pp. 1–20, 2018.

[16] D. Arnold, O. Montenbruck, S. Hackel, and K. Sośnica, "Satellite laser ranging to low Earth orbiters: orbit and network validation," *J. of Geodesy*, vol. 93, pp. 2315—-2334, 2019.

[17] P. Teunissen and O. Montenbruck, Eds., *Springer Handbook of Global Navigation Satellite Systems*. Springer International Publishing AG, 2017.

[18] M. Eineder, C. Minet, P. Steigenberger, X. Cong, and T. Fritz, "Imaging geodesy - Toward centimeter-level ranging accuracy with TerraSAR-X," *IEEE Trans. on Geosci. and Remote Sens.*, vol. 49, no. 2, pp. 661–671, 2011.

[19] X. Cong, U. Balss, M. Eineder, and T. Fritz, "Imaging geodesy - Centimeter-Level Ranging Accuracy With TerraSAR-X: An Update," *IEEE Geosci. and Remote Sens. Lett.*, vol. 9, no. 5, pp. 948–952, 2012.

[20] C. Gisinger, U. Balss, R. Pail, X. Zhu, S. Montazeri, S. Gernhardt, and M. Eineder, "Precise Three-Dimensional Stereo Localization of Corner Reflectors and Persistent Scatterers with TerraSAR-X," *IEEE Trans. on Geosci. and Remote Sens.*, vol. 53, pp. 1782–1802, 2015.

[21] U. Balss, C. Gisinger, and M. Eineder, "Measurements on the Absolute 2-D and 3-D Localization Accuracy of TerraSAR-X," *Remote Sens.*, vol. 10, no. 656, pp. 1–21, 2018.

[22] U. Balss, C. Gisinger, M. Eineder, H. Breit, A. Schubert, and D. Small, "Survey Protocol for Geometric SAR Sensor Analysis," Technical Note by DLR and RSL UZH, Doc. DLR-FRM4SAR-TN-200, Iss. 1.4, Date 26.04.2018, Accessed Oct. 10, 2021, 2018. Accessed: July 4, 2022. [Online]. Available: http://calvalportal.ceos.org/calibration-methods-guidelines.

[23] C. Gisinger, A. Schubert, H. Breit, M. C. Garthwaite, U. Balss, M. Willberg, D. Small, M. Eineder, and N. Miranda, "In-Depth Verification of Sentinel-1 and TerraSAR-X Geolocation Accuracy Using the Australian Corner Reflector Array," *IEEE Trans. on Geosci. and Remote Sens.*, vol. 59, no. 2, pp. 1154—-1181, 2021.

[24] A. Gray, N. Short, K. Mattar, and K. Jezek, "Velocities and flux of the Filchner ice shelf and its tributaries determined from speckle tracking interferometry," *Canadian J. Rem. Sens.*, vol. 27, no. 3, 2001.

[25] I. Joughin, "Ice-sheet velocity mapping: a combined interferometric and speckle-tracking approach," *Annals of Glaciology*, vol. 34, pp. 195–201, 2002.

[26] T. Strozzi, A. Luckman, T. Murray, U. Wegmüller, and C. Werner, "Glacier Motion Estimation Using SAR Offset-Tracking Procedures," *IEEE Trans. on Geosci. and Remote Sens.*, vol. 40, no. 11, pp. 2384—-2391, 2002.

[27] T. Nagler, H. Rott, M. Hetzenecker, J. Wuite, and P. Potin, "The Sentinel-1 Mission: New Opportunities for Ice Sheet Observations," *Rem. Sens.*, vol. 7, no. 7, pp. 9371—-9389, 2015.

[28] C. Meertens, B. Brooks, J. Foster, and M. Miller, "Troposphere, Ionosphere, GPS, and Interferometric Radar (TIGIR) Workshop Proposal," Proposal submitted to NSF EAR Geophysics, Accessed Oct. 10, 2021, 2009. Accessed: July 4, 2022. [Online]. Available: https://www.unavco.org.

[29] B. Rommen, A. Mika, L. Gale, H. Zelle, R. Hanssen, S. Liu, C. Matzler, J. Morland, U. Wegmüller, C. Werner, and M. Santoro, "The ESA METAWAVE project: Correcting for atmospheric water vapour effects in InSAR products," in *3rd European Conference on Antennas and Propagation*, 2009, pp. 3428–3432.

[30] E. Hólm, R. Forbes, S. Lang, L. Magnusson, and S. Malardel, "New model cycle brings higher resolution," ECMWF Newsletter, No. 147, ECMWF, Reading, United Kingdom, Accessed Oct. 10, 2021, pp. 14–19, 2016. Accessed: July 4, 2022. [Online]. Available: http://www.ecmwf.int/sites/default/files/elibrary/2016/16299-newsletter-no147-spring-2016.pdf.

[31] M. Bourbigot, H. Johnsen, and R. Piantanida, "Sentinel-1 Product Definition," Technical note by Sentinel-1 Mission Performance

Center (MPC), Doc. S1-RS-MDA-52-7440, Iss. 2, Rev. 7, Date 25.03.2016, 2016. Accessed: July 4, 2022. [Online]. Available: https://sentinel.esa.int/web/sentinel/user-guides/document-library.

[32] J. C. Curlander, "Location of Spaceborne SAR Imagery," *IEEE Trans. on Geosci. and Remote Sens.*, vol. GE-20, no. 3, 1982.

[33] T. Fritz, L. Krieger, C. Gisinger, and M. Lachaise, "S1-ETAD Project Product Definition Document," ESA Technical Document, Doc. ETAD-DLR-PS-0002, Iss. 2.1, Date 16.06.2021, 2021. Accessed: July 4, 2022. [Online]. Available: https://sentinel.esa.int/web/sentinel/missions/sentinel-1/data-products/etad-dataset.

[34] L. Krieger, T. Fritz, C. Gisinger, and M. Lachaise, "S1-ETAD Project Product Format Specification," ESA Technical Document, Doc. ETAD-DLR-PS-0014, Iss. 1.5, Date 16.06.2021, 2021. Accessed: July 4, 2022. [Online]. Available: https://sentinel.esa.int/web/sentinel/missions/sentinel-1/data-products/etad-dataset.

[35] S. Mbaye and M. Moucha, "Standard Archive Format for Europe SAFE Control Book Volume 1 Core Specification," ESA Technical Document, Doc. PGSI-GSEG-EOPG-FS-05-0001, Iss. 1.0, Date 19.08.2005, 2005.

[36] G. Hajduch, P. Vincent, K. Cordier, M. Grignoux, R. Husson, C. Peureux, R. Piantanida, A. Recchia, N. Francheschi, K. Schmidt, H. Johnsen, A. Mouche, A. Grouazel, F. Collard, and G. Guitton, "S-1A & S-1B Annual Performance Report 2020," ESA Technical Document, Doc. MPC-0504, Iss. 1.1, Date 16.03.2021, 2021. Accessed: July 4, 2022. [Online]. Available: https://sentinel.esa.int/documents/247904/3406423/Sentinel-1-Annual-Performance-Report-2018.pdf.

[37] E. Fahrland, P. Jacob, H. Schrader, and H. Kahabka, "Copernicus Digital Elevation Model Product Handbook," Copernicus Technical Document, Doc. GEO.2018-1988-2, Iss. 3.0, Date 09.11.2020, 2020. Accessed: July 4, 2022. [Online]. Available: https://spacedata.copernicus.eu.

[38] N. Pavlis, S. Holmes, S. Kenyon, and J. Factor, "The development and evaluation of the Earth GravitationalModel 2008 (EGM2008)," *J. of Geophys. Res.*, vol. 117, no. B04406, 2012.

[39] National Imagery and Mapping Agency, "World Geodetic System 1984 - Its Definition and Relationships with Local Geodetic Systems," NIMA Technical Document, Doc. TR8350.2, Iss. 3.1, Date 03.01.2000, 2000.

[40] C. Gisinger, U. Balss, S. Suchandt, and T. Fritz, "S1-ETAD Project Algorithm Technical Baseline Document," ESA Technical Document, Doc. ETAD-DLR-DD-0008, Iss. 2.1, Date 20.04.2020, 2020. Accessed: July 4, 2022. [Online]. Available: https://sentinel.esa.int/web/sentinel/missions/sentinel-1/data-products/etad-dataset.

[41] A. Hofmeister, "Determination of path delays in the atmosphere for geodetic VLBI by means of ray-tracing," PhD Thesis, Technical University of Vienna, 2016. Accessed: July 4, 2022. [Online]. Available: http://katalog.ub.tuwien.ac.at/AC13248753.

[42] ECMWF, *IFS Documentation CY47R3*. ECMWF, 2021. Accessed: July 4, 2022. [Online]. Available: https://www.ecmwf.int/en/publications/ifs-documentation.

[43] J. Wallace and P. Hobbs, *Atmospheric Science: An Introductory Survey, 2nd Edition*. Elsevier Inc., 2006.

[44] E. Smith and S. Weintraubt, "The Constants in the Equation for Atmospheric Refractive Index at Radio Frequencies," *Proc. of the I.R.E.*, vol. 41, no. 8, pp. 1035–1037, 1953.

[45] A. Villiger and R. Dach, Eds., *International GNSS Service Technical Report 2020*. IGS Central Bureau and University of Bern, 2021. Accessed: July 4, 2022. [Online]. Available: https://www.igs.org.

[46] S. Schaer, *Mapping and Predicting the Earth's Ionosphere using the Global Positioning System.*, ser. Geodaetisch-geophysikalische Arbeiten in der Schweiz, vol. 59. Schweizerische Geodaetische Kommission, 1999. Accessed: July 4, 2022. [Online]. Available: http://www.sgc.ethz.ch/publications.

[47] B. Hofmann-Wellenhof, H. Lichtenegger, and E. Wasle, *GNSS Global Navigation Satellite Systems*. Springer Wien NewYork, 2008.

[48] G. Petit and B. Luzum, Eds., *IERS Conventions (2010)*. Verlag des Bundesamts für Kartographie und Geodäsie, 2010. Accessed: July 4, 2022. [Online]. Available: http://tai.bipm.org/iers/conv2010/conv2010.html.

[49] C. Acton, "Ancillary Data Services of NASA's Navigation and Ancillary Information Facility," *Planetary and Space Sci.*, vol. 44, no. 1, pp. 65–70, 1996.

[50] M. Bourbigot, H. Johnsen, and R. Piantanida, "Sentinel-1 Product Specification," Technical note by Sentinel-1 Mission Performance Center (MPC), Doc. S1-RS-MDA-52-7441, Iss. 3, Rev. 6, Date 27.06.2019, 2016. Accessed: July 4, 2022. [Online]. Available: https://sentinel.esa.int/web/sentinel/user-guides/document-library.

[51] ESA, "Reader API for Sentinel-1 Extended Timing Annotation Dataset," Gitlab repository s1-etad maintained by ESA, Accessed Oct. 12, 2021, 2021. Accessed: July 4, 2022. [Online]. Available: https://gitlab.com/s1-etad/s1-etad.

[52] N. Yague-Martinez, P. Prats, F. Gonzalez, R. Brcic, R. Shau, D. Geudtner, M. Eineder, and R. Bamler, "Interferometric Processing of Sentinel-1 TOPS Data," *IEEE Trans. on Geosci. and Remote Sens.*, vol. 54, no. 4, pp. 2220—-2234, 2016.

[53] M. Thankappan, M. Garthwaite, C. Gisinger, A. Schubert, P. Meadows, and N. Miranda, "Improvements to the position coordinates for the Australian corner reflector array and new infrastructure to support SAR calibration and multi-technique validation at the Yarragadee fundamental geodetic station," in *Proc. of CEOS WGCV Workshop 2018, Dec. 5–7, Buenos Aires, Argentina*, 2018.

[54] D. Small, B. Rosich, A. Schubert, E. Meier, and D. Nüesch, "Geometric Validation of Low and High-Resolution ASAR Imagery," in *Proc. of 2004 Envisat ERS Symposium, Sep. 6–10, Salzburg, Austria*, 2005.

[55] A. Schubert, N. Miranda, D. Geudtner, and D. Small, "Sentinel-1A/B Combined Product Geolocation Accuracy," *Remote Sens.*, vol. 9, no. 607, 2017.

[56] U. Balss, X. Y. Cong, R. Brcic, M. Rexer, C. Minet, H. Breit, M. Eineder, and T. Fritz, "High precision measurement on the absolute localization accuracy of TerraSAR-X," in *Proc. of IGARSS'12 Conf., July 22–27, Munich, Germany*, 2012, pp. 1625–1628.

[57] Z. Altamimi, P. Rebischung, L. Métivier, and X. Collilieux, "ITRF2014: A new release of the International Terrestrial Reference Frame modeling nonlinear station motions," *J. of Geophys. Res.*, vol. 121, no. 8, pp. 6109–6131, 2016.

[58] A. Schubert, D. Small, N. Miranda, D. Geudtner, and E. Meier, "Sentinel-1A Product Geolocation Accuracy: Commissioning Phase Results," *Remote Sens.*, vol. 7, pp. 9431–9449, 2015.

[59] R. Bamler and M. Eineder, "Accuracy of Differential Shift Estimation by Correlation and Split-Bandwidth Interferometry for Wideband and Delta-k SAR Systems," *IEEE Geosci. and Remote Sens. Lett.*, vol. 2, pp. 151–155, 2005.

[60] R. Czikhardt, H. van der Marel, F. J. van Leijen, and R. F. Hanssen, "Estimating signal-to-clutter ratio of insar corner reflectors from sar time series," *IEEE Geosci. and Remote Sens. Lett.*, vol. Early Access, pp. 1–5, 2021.

[61] Climate Change Service, "Greenland ice sheet annual gridded velocity data from 2017 to present derived from satellite observations," Climate Data Store maintained by ECMWF, Accessed Oct. 12, 2021, 2021. Accessed: July 4, 2022. [Online]. Available: https://doi.org/10.24381/cds.0b96b838.

[62] R. Michel, J. Avouac, and J. Taboury, "Measuring ground displacements from SAR amplitude images: Application to the Landers Earthquake," *Geophys. Res. Letters*, vol. 26, no. 7, pp. 875–878, 1999.

[63] Y. Fialko, M. Simons, and D. Agnew, "The complete (3-D) surface displacement field in the epicentral area of the 1999 MW7.1 Hector Mine Earthquake, California, from space geodetic observations," *Geophys. Res. Letters*, vol. 28, no. 16, pp. 3063–3066, 2001.

[64] M. Tobita, M. Murakami, H. Nakagawa, H. Yarai, S. Fujiwara, and P. A. Rosen, "3-D surface deformation of the 2000 Usu Eruption measured by matching of SAR images," *Geophys. Res. Letters*, vol. 28, no. 22, pp. 4291–4294, 2001.

[65] A. L. Gray, K. E. Mattar, and G. Sofko, "Influence of ionospheric electron density fluctuations on satellite radar interferometry," *Geophys. Res. Lett.*, vol. 27, no. 10, pp. 1451–1454, 2000.

[66] F. Rocca, "Modeling Interferogram Stacks," *IEEE Trans. on Geosci. and Remote Sens.*, vol. 45, no. 10, pp. 3289–3299, 2007.

[67] P. S. Agram and M. Simons, "A noise model for InSAR time series," *J. of Geophys. Res.: Solid Earth*, vol. 120, no. 4, pp. 2752–2771, 2015.

[68] R. Hanssen, *Radar Interferometry: Data Interpretation and Error Analysis*. Kluwer Academic, Dordrecht, Boston, 2001.

[69] N. Adam, "Methodology of a Troposphere Effect Mitigation Processor for SAR Interferometry," *IEEE J. of Sel. Topics in Applied Earth Observations and Remote Sens.*, vol. 12, no. 12, pp. 5334–5344, 2019.

[70] T. R. Lauknes, "InSAR Tropospheric Stratification Delays: Correction Using a Small Baseline Approach," *Geophys. Res. Lett.*, vol. 8, no. 6, pp. 1070–1074, 2011.

[71] A. Ferretti, C. Prati, and F. Rocca, "Permanent scatterers in SAR interferometry," *IEEE Trans. on Geosci. and Remote Sens.*, vol. 39, no. 1, pp. 8–20, 2001.

[72] P. Berardino, G. Fornaro, R. Lanari, and E. Sansosti, "A new algorithm for surface deformation monitoring based on small baseline differential SAR interferograms," *IEEE Trans. on Geosci. and Remote Sens.*, vol. 40, no. 11, pp. 2375–2383, 2002.

[73] T. R. Emardson, M. Simons, and F. H. Webb, "Neutral atmospheric delay in interferometric synthetic aperture radar applications: Statistical description and mitigation," *J. of Geophys. Res.: Solid Earth*, vol. 108, no. B5, pp. 1–8, 2003.
[74] A. Parizzi, R. Brcic, and F. De Zan, "InSAR Performance for Large-Scale Deformation Measurement," *IEEE Trans. on Geosci. and Remote Sens.*, vol. 59, no. 10, pp. 8510–8520, 2021.
[75] G. Gomba, A. Parizzi, F. De Zan, M. Eineder, and R. Bamler, "Toward Operational Compensation of Ionospheric Effects in SAR Interferograms: The Split-Spectrum Method," *IEEE Trans. on Geosci. and Remote Sens.*, vol. 54, no. 3, pp. 1446–1461, 2016.
[76] Blasco Delgado, J.M., "Extending the Sentinel-1 Timing Annotation Datasets using the ESA S1-ETAD service," Service note on ETAD early access in GEP platform, Accessed Oct. 12, 2021, 2021. Accessed: July 4, 2022. [Online]. Available: https://discuss.terradue.com/.

Christoph Gisinger received the Diploma degree in geodesy in 2010 from Technische Universität Graz, Graz, Austria, and in 2012 the M.Sc. degree in earth oriented space science and technologies, and the PhD degree in geodesy in 2019, both from Technische Universität München, Munich, Germany.

Since 2017 he is with the Remote Sensing Technology Institute, German Aerospace Center (DLR), Oberpfaffenhofen, Germany, where he is involved in the geodetic SAR processing of the missions TerraSAR-X and Sentinel-1. His research interests include positioning with SAR, correction modeling for absolute SAR observations, and radargrammetric image processing with a focus on fusing SAR with geodetic observations for new applications.

Ludivine Libert received the Master's degree in Space Sciences from the Université de Liège, Liège, Belgium in 2014. She received her PhD degree in Remote Sensing from the Université de Liège, Liège, Belgium in 2018.

During her PhD, she spent four years with the Centre Spatial de Liège and studied SAR and SAR interferometry, with a focus on multi-spectral and multi-temporal InSAR techniques for deformation monitoring. In 2019, she became a research scientist at ENVEO where her work focused on SAR and InSAR methods for ice and snow monitoring.

Petar Marinkovic received the M.Sc. degree in geodesy from the University of Belgrade, Serbia, in 1999 and from 2002 until 2008 he did PhD studies in the field of physical geodesy and satellite radar interferometry at University of Stuttgart, Germany and Technical University of Delft, The Netherlands. Early 2009 he founded PPO.labs and has been leading it since. PPO.labs is an R&D consultancy company focusing on algorithmic and operational development for ground motion estimation using SAR interferometry.

Lukas Krieger received the B.Sc. degree in computer science from the Technische Universität München, Munich, Germany, in 2011, the M.Sc. degree in health informatics from the Karolinska Institutet, Stockholm, Sweden, in 2013, and the Ph.D. degree from the faculty of aerospace and geodesy of the Technische Universität München, Munich, Germany, in 2020. In 2015, he joined the Remote Sensing Technology Institute, German Aerospace Center (DLR), Oberpfaffenhofen, Germany. His research interests include correction modeling for absolute SAR observations, geodetic mass balance calculations for glaciers and ice sheets and detection of the glacier grounding line with InSAR using the missions TerraSAR-X, TanDEM-X and Sentinel-1.

Yngvar Larsen received the M.Sc. degree in applied physics and the Ph.D. degree in physics from the University of Tromsø, Norway, in 1999 and 2003, respectively. Since 2007, he is with NORCE (formerly Norut) as a Senior Researcher in the Earth Observation group. His current research interests include fundamental signal processing for SAR and interferometric SAR, including in particular focusing algorithms for new SAR missions and ground motion estimation using SAR interferometry.

Antonio Valentino received the Master's degree in electronic engineering from Politecnico di Torino, Torino, Italy, in 2000. Since 2001, he has been working on Synthetic Aperture Radar (SAR) processing, calibration and applications. He worked on important international SAR missions, including COSMO-SkyMed, Sentinel-1, SAOCOM and BIOMASS. He is currently contractor at the European Space Research Institute (ESRIN), European Space Agency (ESA), Frascati, Italy. He is Sentinel-1 SAR engineer working on calibration and SAR data quality.

Helko Breit received the Diploma degree in electrical and telecommunication science from the Technical University of Munich, Munich, Germany, in 1990. Since 1990, he has been with the German Aerospace Center (DLR), Weßling, Germany, where he is currently supervising the synthetic aperture radar (SAR) processor development team at the Remote Sensing Technology Institute.

He has worked on a variety of international missions, including SIR-C/X-SAR, SRTM/X-SAR, and the German missions TerraSAR-X/TanDEM-X. He contributed to several European Space Agency studies and supported the commissioning of the ESA's Sentinel 1 SAR satellites. He was responsible for the development of the TerraSAR-X multimode SAR processor TMSP and the bi-static processing of TanDEM-X mission data. His current research activities comprise the development of SAR processing algorithms and systems for future SAR satellites and missions.

Ulrich Balss received the Diploma degree in physics and the Dr. phil. nat. degree from the Johann Wolfgang Goethe University, Frankfurt am Main, Germany in 1994 and 2004, respectively.

Between 2003 and 2010, he was with the scientific staff of the Technical University Munich, Munich, Germany. In this time, he worked within the framework of a cooperation of the Technical University Munich and the German Aerospace Center (DLR), and he was permanently located at the Remote Sensing Technology Institute (IMF) of the DLR. In 2010, he joined DLR's Remote Sensing Technology Institute. He is involved in the German TerraSAR-X and TanDEM-X missions. In particular, he participated in the development of the TerraSAR-x Multimode SAR Processor (TMSP) and implemented the focusing kernel of the TMSP.

Steffen Suchandt received the Dipl.-Ing. degree in electrical engineering from the University of Rostock, Germany, in 1995. From 1996 to 1998, he was with the Hochschule Wismar, Germany, working on audiometry and otoacoustic emissions. Since 1998, he has been with the Remote Sensing Technology Institute of the German Aerospace Center (DLR), Oberpfaffenhofen, Germany, working on numerous aspects of synthetic aperture radar (SAR). He was engaged in processor development and data calibration for the Shuttle Radar Topography Mission SRTM/X-SAR, was responsible for the development of a traffic data extraction system for the TerraSAR-X mission and he was a system engineer in design and development of the SAR geodesy processor SGP and the Sentinel-1 extended timing annotation data processor SETAP. He has wide experience in SAR interferometry, signal and image processing and in software design. His current research is focused on multi-channel space borne SAR oceanography and on SAR geodesy.

Thomas Nagler received the M.Sc. degree in meteorology and the Ph.D. degree in natural sciences from the University of Innsbruck, Innsbruck, Austria, in 1991 and 1996, respectively.

From 1991 to 2004, he was a Research Scientist with the Institute of Meteorology and Geophysics, University of Innsbruck. He is a Cofounder and, since 2001, Managing Director of Environmental Earth Observation Information Technology (ENVEO IT) GmbH, Innsbruck. He has been a Principle/Coinvestigator and Coordinator for several projects of ESA, the European Commission, and the Austrian Research Promotion Agency. He is/was a member of the Mission Advisory Group for Copernicus ROSE-L and Sentinel-1-NG. He has participated in several scientific expeditions to Patagonia, Antarctica, and Alpine Glaciers, and was leading/participating in international field campaigns in preparation for new satellite systems. His main research interests include retrieval methods and applications of microwave and optical remote sensing for snow hydrology, climatology, monitoring Alpine and polar glaciers and ice sheets, and assimilation of remote sensing products into geophysical process models.

Michael Eineder received the Diploma degree in electrical engineering from Technische Universität München (TUM), München, Germany, in 1990 and the Dr. rer. nat. degree from the University of Innsbruck, Innsbruck, Austria, in 2004.,Since 2013, he has been an honorary Professor with TUM, where he is also currently a part-time Lecturer of remote sensing. He is also currently the Head of the SAR signal processing department of the Remote Sensing Technology Institute, German Aerospace Center (DLR), Wessling, Germany.

His responsibilities encompass the development of SAR and interferometric SAR processing systems for current and future radar missions. Since 1990, he has been with DLR, where he has worked on a variety of international missions, including SIR-C/X-SAR, SRTM/X-SAR in cooperation with the National Aeronautics and Space Administration, ERS-1 (European Space Agency), and TerraSAR-X and TanDEM-X (Germany). His current research interest is focused on future SAR missions and on imaging geodesy, an absolute positioning technique exploiting high-resolution SAR.

Nuno Miranda received the Master's degree in telecommunications engineering from the University of Bordeaux, Talence, France, in 1999. Since 2000, he has been working on synthetic aperture radar (SAR) application (interferometry) and calibration.

He is currently with the European Space Research Institute (ESRIN), European Space Agency (ESA), Frascati, Italy. He is responsible for algorithm and processor development and calibration for the ESA SAR missions (ERS, ASAR, and Sentinel-1).